Applied Thermal Engineering 235 (2023) 121353

Contents lists available at ScienceDirect

Applied Thermal Engineering

journal homepage: www.elsevier.com/locate/apthermeng

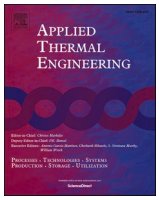

Research Paper

# Numerical study on thermal performance and thermal stress of molten salt receiver tube based on induction heating

Ao Zhang, Yuhang Zuo, Mingrui Zhang, Hao Zhou *

*State Key Laboratory of Clean Energy Utilization, Institute for Thermal Power Engineering, Zhejiang University, Hangzhou 310027, China*

ARTICLE INFO

*Keywords:*
Induction heating
Receiver tube
Preheating
Salt circulating
Thermal stress

ABSTRACT

Induction heating is an emerging research method that can recreate half-perimeter heating of a receiver tube in a tower-concentrating solar power plant. In this study, a three-dimensional (3D) field numerical model that couples electromagnetic induction, heat transfer, and turbulence, is developed to study the thermal performance of a receiver tube during the preheating process and under salt circulation conditions. The effects of the coil-to-tube distance, coil power, molten salt inlet temperature, molten salt inlet velocity, and ambient temperature were investigated. Furthermore, the thermal stress distribution and evolution in the tube were calculated. The heat generation was fund to be concentrated on the outer surface of the tube front. The increase in coil power significantly accelerated the preheating process. With increase in the coil power from 200 to 500 W, the time required for the maximum tube temperature to reach 350 °C reduced by 55.67 %. The heating efficiency increased with increasing coil power, molten salt inlet velocity, and ambient temperature decreased with increasing coil-to-tube distance and molten salt inlet temperature. Among them, the molten salt inlet temperature had a more significant effect. As it increased from 250 to 400 °C, the heating efficiency decreased from 47.17 to 18.82 %. The maximum and minimum equivalent thermal stresses at preheat stabilization were reached at $\theta = 0^{\circ}$ and $\theta = 45^{\circ}$, respectively. Furthermore, the equivalent thermal stress at preheat stabilization differed from that with salt circulation by only 4.46 %.

## 1. Introduction

Global warming, caused by increasing $CO_2$ emissions, significantly affects human habitats. Renewable energy is crucial to the tough process of achieving "carbon neutrality" by effectively reducing human dependence on traditional fossil energy sources and slowing the rate of $CO_2$ emissions [1,2]. Solar thermal technology has become among the most popular renewable energy sources because it does not produce pollutants during operation and can overcome the inherent volatility and intermittency of renewable energy sources [3,4]. Tower concentrated solar power (CSP) plants, which use molten salt (MS) as a heat transfer fluid, are well suited for large-scale, large-capacity commercial applications owing to their high concentration ratio, high operating temperature, and low heat loss. This is also the mainstream trend for the construction of solar thermal power plants in the coming period [5,6]. A schematic of the most common MS tower CSP plant is shown in Fig. 1. One of the most critical devices is the receiver, which converts solar energy into thermal energy, which is essential for the effective and secure operation of power plants. The most widely used receiver in tower CSP plants is the external cylindrical receiver as it can receive energy in all directions [7]. This type of receiver widely uses Solar Salt (60 wt % $NaNO_3$ – 40 wt % $KNO_3$) as a heat transfer fluid, which is heated from 290 °C to 565 °C in the receiver.

The thermal performance of a receiver significantly affects the operating efficiency of CSP tower plants. In addition, during the operation of a receiver, its front side is exposed to unstable and nonuniform heat flow, and the huge temperature difference can lead to excessive thermal stress, which can cause damage to the tubes. Therefore, the analysis and evaluation of the thermal performance and thermal stress of a receiver is also a hot research topic. Yu et al. [8] modeled a MS receiver with a cylindrical structure and investigated the effects of critical parameters on thermal performance. The surface heat flux, ambient wind velocity, and absorptance were observed to significantly affect the thermal performance. Qaisrani et al. [9,10] numerically investigated the heat loss and thermal performance of rectangular and cylindrical receivers. The wind retaining wall can effectively reduce the convective heat loss; however, radiation was the primary cause of heat loss from the receiver. Emerick et al. [11] developed a numerical model to optimize the configuration of a receiver utilizing supercritical carbon dioxide as

* Corresponding author at: State Key Laboratory of Clean Energy Utilization, Zhejiang University, Zheda Road 38, Hangzhou 310027, China.
*E-mail address:* zhouhao@zju.edu.cn (H. Zhou).

https://doi.org/10.1016/j.applthermaleng.2023.121353
Received 28 May 2023; Received in revised form 9 July 2023; Accepted 11 August 2023
Available online 12 August 2023

**Nomenclature**

*Greek symbols*

| | |
|---|---|
| $\alpha$ | linear thermal expansion coefficient ($K^{-1}$) |
| $\varepsilon$ | surface emissivity |
| $\eta$ | efficiency |
| $\theta$ | cylindrical coordinate (rad) |
| $\mu$ | viscosity (Pa•s) |
| $\nu$ | Poisson's ratio |
| $\rho$ | density ($kg/m^3$) |
| $\sigma$ | Stephen Boltzmann constant ($W/(m^2 \cdot K^4)$) |
| $\sigma_r$ | radial thermal stress (MPa) |
| $\sigma_\theta$ | circumferential thermal stress (MPa) |
| $\sigma_z$ | axial thermal stress (MPa) |
| $\sigma_{eq}$ | equivalent thermal stress (MPa) |
| $\sigma_e$ | electrical conductivity (S/m) |
| $\omega$ | angular frequency of the magnetic field (rad/s) |
| $\Delta$ | difference |

*Roman symbols*

| | |
|---|---|
| **A** | magnetic vector potential (V•s/m) |
| **B** | magnetic flux density vector (T) |
| B | Fourier coefficient |
| $C_p$ | specific heat (J/(kg•K)) |
| **D** | electric flux density vector ($C/m^2$) |
| D | Fourier coefficient |
| d | hydraulic diameter (mm) |
| **E** | electric field intensity vector (V) |
| E | Young's modulus (GPa) |
| **H** | magnetic field intensity vector (A/m) |
| $h$ | convection coefficient ($W/(m^2 \bullet K)$) |
| **J** | electric current density ($A/m^2$) |
| K | geometric thermal stress term (K) |
| k | thermal conductivity (W/(m·K)) |
| $L$ | coil - to - tube distance (mm) |
| $P$ | coil power (W) |
| $Q$ | heat generation (W) |
| $q$ | heat flux ($W/m^2$) |
| R | radius (mm) |
| $r$ | radial coordinate (mm) |
| $T$ | temperature (K) |
| $\overline{T}$ | average temperature (K) |
| $t$ | time (s) |
| $v$ | molten salt inlet velocity (m/s) |
| $z$ | axial coordinate (mm) |

*Abbreviations*

| | |
|---|---|
| CFD | computational fluid dynamics |
| CSP | concentrating solar power |
| MS | molten salt |

*Subscripts*

| | |
|---|---|
| amb | ambient |
| b | boundary |
| c | coil |
| e | electric |
| eq | equivalent |
| i | inner wall |
| in | inlet |
| max | maximum |
| min | minimum |
| ml | magnetic loss |
| o | outer wall |
| out | outlet |
| rh | resistive loss |
| s | salt |
| t | tube |
| w | water |
| $r$ | radial component |
| $z$ | axial component |
| $\theta$ | circumferential component |

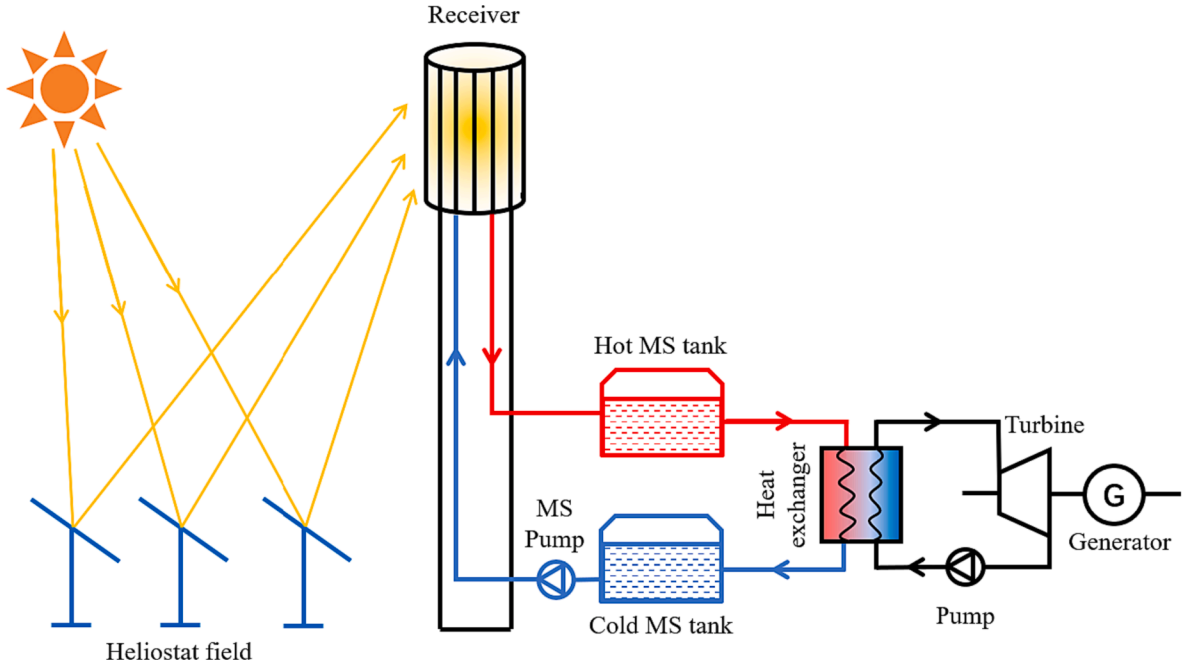


**Fig. 1.** Schematic diagram of tower CSP plant.

the working medium. By assuming a constant external area of the receiver and varying the number of plates, they determined a design that maximizes the efficiency. Erasmus et al. [12] investigated a novel central receiver technology employing a tessellated array of heat transfer units and analyzed its thermal performance and thermal efficiency. This study estimated the receiver's capacity to achieve an outlet temperature of 800 °C while maintaining a thermal efficiency of 59 %. Du et al. [13] simulated the thermal stress and fatigue fracture of a receiver, and derived a minimum heat flow density equation for the occurrence of damage on a wall surface. The results indicated that the thermal stress distribution was similar to the radial temperature difference and that the maximum stress occurred at the outer wall of the tube. Peng et al. [14] numerically analyzed the effect of tube size on thermal stress distribution. The results indicated that the tube wall thickness had a more significant effect than the tube diameter. Zuo et al. [15] numerically studied the preheating process of a receiver tube. The results showed that wind blowing from the 30° direction had the greatest effect. The preheating time under windless conditions was 63.96 % shorter than that under windless conditions. Pérez-Álvarez et al. [16,17] numerically investigated the effects of mechanical attachment and eccentricity on the temperature distribution and thermomechanical performance of a central receiver. The study revealed that considering all the mechanical attachments is essential for accurately calculating the tube's temperature. Furthermore, the eccentric tubes effectively enhanced the heat transfer efficiency and reduced thermal stress.

In summary, most studies on the thermal performance and thermal stress of receivers in tower CSP plants have been conducted using numerical simulations. In contrast, experimental studies on receivers are scarce. This is primarily owing to the extreme operating conditions of a receiver and the challenges in obtaining receiver data, making it difficult to experimentally measure the thermomechanical properties of a receiver. Moreover, the inadequate light source conditions during experiments hinder the accurate replication of the complex and nonuniform heat flux on the surface of receivers. Additionally, the solidification of the MS further complicates the construction of an experimental system. The use of electromagnetic induction in heat receiver tubes is an emerging experimental method. This technique can provide high heat generation in a controlled and rapid manner and facilitate the gathering of the induced heat to a specified area of the workpiece [18], which can effectively restore the scenario of a half-perimeter of the receiver tube being heated and solve the difficult problem in the experiment effectively. It is a non-contact heating method with low cost and a relatively simple experimental system. In this technology, a high-frequency alternating current (AC) passes through an induction coil, which generates an eddy current on the workpiece surface. These eddy currents generate Joule heat to heat the workpiece. Several studies have examined the electromagnetic induction heating of MS.

Wang et al. [19] designed an experimental device for a spherical bed using induction heating to provide an internal heat source for studying the forced convective heat transfer characteristics of the MS on a heat transfer salt circulation. Zhang et al. [20] built an experimental system for the induction heating of MS and compared the experimental results with the simulation results. Fernández-Torrijos et al. [21] designed an MS circulation experimental system with an induction heater and investigated the heat transfer process. The results revealed that the temperature increased significantly in the tube region facing the induction heater coil, whereas the rear of the tube remained almost unaffected. Further, Fernández-Torrijos et al. [22] used the same experimental system to develop a 2D numerical model of an MS circular tube flow under nonuniform circumferential heat flow and used an inverse heat transfer method to derive the heat flow on the tube based on the outer surface temperature. The results showed that the temperature obtained using the inverse heat transfer method was consistent with the experimental results. Fernández-Torrijos et al. [23] conducted an experimental study on the start-up process of a receiver tube using an induction heater. A 3D numerical model of a hollow circular tube under the action of a nonuniform heat flow was developed to analyze the displacement and thermal stress of the tube during the start-up of the receiver. The thermal stress in the empty tube was observed to be greater than that in the case of the MS flow in the tube. Rodríguez-Sanchez et al. [24] used an induction heating system to obtain nonuniform heat fluxes on a tube, measured the temperature and displacement of the tube, and calculated its strain field. The results showed that the heating power had a significant effect on the tube temperature distribution, whereas the fluid mass flow rate exerted minimal effects. Cano-Pleite et al. [18] developed a 2D numerical model coupled with electromagnetic and heat transfer physical fields to simulate the induction heating of a receiver tube. They investigated the heat generation depth and temperature distribution of the tube. The results showed that induction heating exhibits a volumetric nature and that no surface heat flow produces the same temperature distribution. Nevertheless, there exists a notable research gap when it comes to employing induction heating to simulate the heating of half the perimeter of the receiver tube. The practicality and efficiency of this approach are yet to be verified. Hence, while carrying out experimental studies, it becomes imperative to complement them with simulation research to acquire more comprehensive data. By mutually corroborating the findings with experimental studies, simulation research can offer valuable insights for experimental design and parameter selection, thereby augmenting the overall breadth and depth of research in this field.

Overall, to simulate the heating of a receiver tube at half circumference in a tower CSP power plant, an induction coil can be positioned on one side of the receiver tube, thus solving the experimental difficulty and achieving the desired heating effect. Due to the scarcity of literature on this specific topic, simulation studies are crucial for validation and offering guidance to experimental investigations. Most existing simulation studies focus on calculating the heat flow on the tube surface using inverse heat transfer methods, without coupling the electromagnetic field. The current numerical model that couples the electromagnetic physical field is 2D; therefore, convective heat transfer is not simulated. Rather, it is represented by the corresponding internal and external flow boundary conditions. Few 3D simulation studies have been conducted using electromagnetic induction to generate circumferentially nonuniform heat to heat receiver tubes. In this paper, induction heating is used to restore the scenario of the half circumference of the receiver tube being heated in tower CSP plants. A novel 3D multi-physical field model that couples electromagnetic induction, heat transfer, and turbulence is developed to study the thermal performance and mechanical performance of a MS receiver tube. An experimental system for electromagnetic induction heating of a receiver tube was constructed to verify the model. The effects of critical factors such as the coil-to-tube distance, coil power and ambient temperature on the induction heating process were investigated. Finally, the tube thermal stress was calculated using a 2D thermoelastic analytical model.

## 2. Numerical model and validation

### 2.1. Numerical model

A commercial CFD software - COMSOL Multiphysics® - was used to build a 3D numerical model, a schematic of which is shown in Fig. 2. In this model, electromagnetic induction was used to heat the tube half circumference of the tube to simulate the nonuniform heat flow provided by sunlight. As shown in Fig. 2(a), the model comprises a receiver tube and an induction heater. To simplify the model and correspond to the experiment, a 330 mm long receiver tube and corresponding induction heater were established for the numerical study. The induction heater and receiver tube were surrounded by a cylindrical air domain with a radius and height of 150 and 330 mm, respectively, and an infinite element domain with a thickness of 5 mm was set up to simulate the surrounding atmosphere. To simplify the model, the remaining structures of the induction heater, special varnish covering the copper

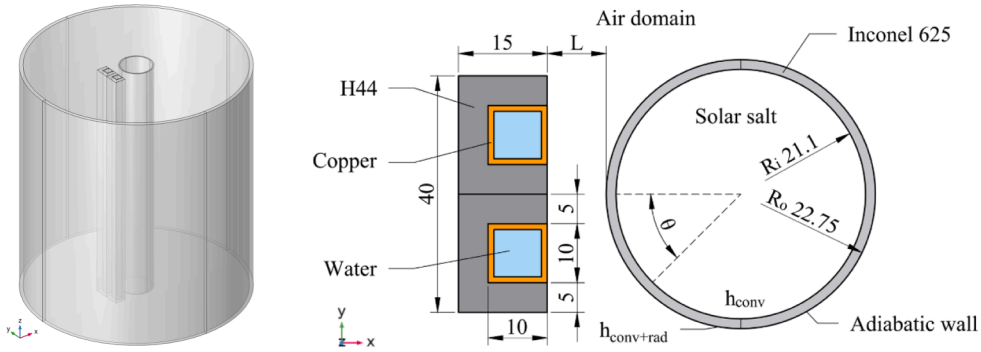


(a) 3D model schematic (b) Schematic diagram of the model cross-section

**Fig. 2.** Schematic diagram of the numerical model.

coils and magnetic flux concentrators, and thermocouples on the receiver tube were not included in the model. Fig. 2(b) shows a cross-sectional schematic of the induction heater and the receiver tube. The receiver tube was made of Inconel 625 alloy with inner and outer diameters of 42.2 and 45.5 mm, respectively. Under preheating conditions, the area inside the tube was air. In the salt-circulating condition, Solar Salt flowed inside the tube along the positive direction of the z-axis. The cross-section of the induction heater was 40 mm long and 15 mm wide and comprised two identical rectangular copper coils wrapped with magnetic flux concentrators. The rectangular copper coil had cross-sectional dimensions of 10 mm × 10 mm and a thickness of 1 mm. The distance between the coil and tube is denoted as *L*. Magnetic flux concentrators with a thickness of 5 mm were wrapped around the coils on three sides except for the side facing the tube. Magnetic flux concentrators were used on ferrite H44, which has high magnetic permeability. Their presence ensured that the magnetic field was concentrated on the side of the coils facing the tube, thereby improving the heating efficiency. Cooling water was passed inside the coils to prevent damage to the induction heater owing to high temperatures during operation. Once induction heating started, a 300 kHz high-frequency alternating current was passed through the rectangular copper coils, generating an alternating magnetic field. The magnetic field induces a current on the surface of the receiver tube, which generates heat that increases the tube temperature.

The variations in the physical properties of the Solar Salt and Inconel 625 alloy with temperature were considered owing to the considerable temperature variations in the receiver tube and MS during the heating process. Table 1 lists the thermal properties of Solar Salt[25], and Table 2 lists the physical properties of Inconel 625 alloy, copper and H44 [15,18]. The initial relative permeability of the magnetizer was 3000; however, the relative permeability of the magnetizer was set to 10,000 because the permeability of the induction heater will be much larger than the initial permeability when it is turned on [18]. Table 3 lists all simulation cases. In the preheating cases, cases pre_1–pre_4 studied the effect of the coil-to-tube distance *L*. Cases pre_5–pre_7 studied the effect of the coil power *P* compared with case pre_1. In the salt-circulating cases, cases salt_1–salt_4 studied the effect of the coil-to-tube distance *L*. Cases salt_5–salt_7 studied the effect of the coil power *P* compared with case salt_1. Cases salt_8–salt_10 studied the effect of the MS inlet temperature $T_{s,in}$ compared with salt_1. Further, cases salt_11–salt_13 studied the effect of the MS inlet velocity $v_{s,in}$, compared with salt_1. Cases salt_14–salt_16 studied the effect of ambient temperature $T_{amb}$ compared with salt_1.

### 2.1.1. Thermal model

In this model, heat is generated at the surface of the tube wall by electromagnetic induction and conducted in all directions. Then, heat is transferred to the air by natural convection and radiation and to the MS inside the tube by forced convection. The corresponding heat conduction equation is expressed as

$$\rho C_p \frac{\partial T}{\partial t} + \nabla \bullet \boldsymbol{q} = Q_e + Q_b \tag{1}$$

$$\boldsymbol{q} = -k_t \nabla T \tag{2}$$

where $\rho$ is the density of the tube, $C_p$ is the specific heat of the tube, $T$ is the temperature at any point on the tube wall, $k_t$ is the thermal conductivity of the tube, $Q_e$ is the heat generated by the induced current inside the tube wall, and $Q_b$ is the heat losses at the domain boundaries. This study created a 3D model to facilitate the coupling and subsequent calculation of the heat transfer between the MS and tube wall. For the inner surface of the tube, the Kay–Crawford heat transfer turbulence model was adopted for the heat transfer calculation between the MS and tube. The outer surface of the rear side of the tube was set as an adiabatic boundary. The front side of the receiver tube dissipates heat via natural convection and thermal radiation. The tube surface emissivity $\varepsilon$ was set to 0.8 because the receiver in a tower CSP plant is typically black. The heat dissipation on the outer surface of the tube can be expressed as

$$q_o = h_o(T_o - T_{amb}) + \varepsilon\sigma(T_o^4 - T_{amb}^4) \tag{3}$$

where $h_o$ is the convective heat transfer coefficient, $T_o$ is the temperature of the outer surface of the tube, $T_{amb}$ is the ambient temperature, and $\sigma$ is the Stephen–Boltzmann constant. In addition, the heat transfer between the coil and internal cooling water was not the object of this study; therefore, the temperature of the cooling water was not calculated. However, the cooling water temperature was assumed to be

**Table 1**
The thermal properties of Solar Salt [25].

| Physical properties | Unit | Value |
|---|---|---|
| Specific heat | J/(kg•K) | $1396 + 0.172 \bullet T$ |
| Density | kg/m$^3$ | $2263.7–0.636 \bullet T$ |
| Thermal conductivity | W/(m•K) | $0.391 + 0.00019 \bullet T$ |
| Viscosity | Pa•s | $0.0755–2.776 \bullet 10^{-4} \bullet T + 3.489 \bullet 10^{-7} \bullet T^2 - 1.474 \bullet 10^{-10} \bullet T^3$ |

$T$ - The temperature of the Solar Salt (K).

**Table 2**
The physical properties of Inconel 625, copper and H44.

| Material | Thermal conductivity [W/(m•K)] | Specific heat [J/(kg•K)] | Density [kg/m$^3$] | Electrical conductivity [S/m] | Relative permeability [-] |
|---|---|---|---|---|---|
| Inconel 625[15] | 2.937 + 0.02• $T$ | 308.81 + 0.247• $T$ | 8890 | 7.8•10$^5$ | 1 |
| Copper | 400 | 385 | 8940 | 5.998•10$^7$ | 1 |
| H44[18] | 0.0353 | 800 | 4800 | 0.154 | 10,000 |

$T$ - The temperature of the Inconel 625 alloy (K).

**Table 3**
Simulation cases.

| Case | | Coil-to-tube distance (mm) | Coil Power (W) | MS inlet temperature (°C) | MS inlet velocity (m/s) | Ambient temperature (°C) |
|---|---|---|---|---|---|---|
| Preheating | pre_1 | 10 | 200 | – | – | 20 |
| | pre_2 | 5 | 200 | – | – | 20 |
| | pre_3 | 15 | 200 | – | – | 20 |
| | pre_4 | 20 | 200 | – | – | 20 |
| | pre_5 | 10 | 300 | – | – | 20 |
| | pre_6 | 10 | 400 | – | – | 20 |
| | pre_7 | 10 | 500 | – | – | 20 |
| With salt circulating | salt_1 | 10 | 500 | 300 | 0.1 (0.26 kg/s) | 20 |
| | salt_2 | 5 | 500 | 300 | 0.1 | 20 |
| | salt_3 | 15 | 500 | 300 | 0.1 | 20 |
| | salt_4 | 20 | 500 | 300 | 0.1 | 20 |
| | salt_5 | 10 | 750 | 300 | 0.1 | 20 |
| | salt_6 | 10 | 1000 | 300 | 0.1 | 20 |
| | salt_7 | 10 | 1250 | 300 | 0.1 | 20 |
| | salt_8 | 10 | 500 | 250 | 0.1 | 20 |
| | salt_9 | 10 | 500 | 350 | 0.1 | 20 |
| | salt_10 | 10 | 500 | 400 | 0.1 | 20 |
| | salt_11 | 10 | 500 | 300 | 0.2 (0.52 kg/s) | 20 |
| | salt_12 | 10 | 500 | 300 | 0.3 (0.78 kg/s) | 20 |
| | salt_13 | 10 | 500 | 300 | 0.4 (1.04 kg/s) | 20 |
| | salt_14 | 10 | 500 | 300 | 0.1 | −20 |
| | salt_15 | 10 | 500 | 300 | 0.1 | 0 |
| | salt_16 | 10 | 500 | 300 | 0.1 | 40 |

constant at 20 °C. The turbulent heat transfer equation proposed by Sieder and Tate [26] was adopted to set the corresponding internal convective boundary conditions on the inner surface of the coil.

$$q_w = h_w(T_c - T_w) \tag{4}$$

$$h_w = \frac{k_w}{d}0.027Re_D^{\frac{4}{5}}Pr^{\frac{1}{3}}\left(\frac{\mu}{\mu_t}\right)^{0.14} \tag{5}$$

where $T_c$ is the temperature of the coil, $T_w$ is the temperature of the circulating cooling water, $k_w$ is the thermal conductivity of the cooling water, d is the hydraulic diameter, and $\mu$ and $\mu_t$ are the viscosity of the cooling water under the membrane and tube wall temperature conditions, respectively.

### 2.1.2. Electromagnetic model

During the operation of the induction heater, the electromagnetic field in the model can be represented by Maxwell's equations.

$$\nabla \times \mathbf{H} = \mathbf{J} \tag{6}$$

$$\mathbf{B} = \nabla \times \mathbf{A} \tag{7}$$

$$\mathbf{J} = \sigma_e\mathbf{E} + j\omega\mathbf{D} \tag{8}$$

$$\mathbf{E} = -j\omega\mathbf{A} \tag{9}$$

where **H** is the magnetic field intensity,**J** is the electric current density, **B** is the magnetic flux density,**A** is the magnetic vector potential, **E** is the electric field intensity, **D** is the electric flux density, $\sigma_e$ is the electrical conductivity, and $\omega = 2\pi f$ is the angular frequency of the magnetic field. The physical fields of the magnetic field and heat transfer were coupled to calculate the electromagnetic heat. The Joule heat $Q_e$ generated by the induced current is introduced into Eq. (1) as the heat source, as follows:

$$Q_e = Q_{rh} + Q_{ml} \tag{10}$$

where the resistive loss is expressed as $Q_{rh} = \frac{1}{2}\mathrm{Re}(\boldsymbol{J} \bullet \boldsymbol{E}^*)$ and the magnetic loss is expressed as $Q_{ml} = \frac{1}{2}\mathrm{Re}(i\omega\boldsymbol{B} \bullet \boldsymbol{H}^*)$. Joule heat is generated and conducted within the tube wall, causing the tube temperature to increase, and heat is then transferred to the heat-transfer fluid by convection. The induction heating process is calculated by coupling the above electromagnetic and thermal model equations inside COMSOL Multiphysics®.

### 2.1.3. 2D thermoelastic analytical model

In the calculation of the thermal stress in hollow cylindrical tubes, the 2D thermoelastic analytical model additionally considers the contribution of circumferential temperature gradients to the thermal stress, in contrast to the one-dimensional (1D) thermoelastic analytical model. During preheating and salt circulation in the receiver, the circumferential temperature gradient of the tube was significantly greater than the radial temperature gradient. If a 1D thermoelastic analytical model is used, the thermal stress is underestimated. Therefore, the 2D thermo-elastic analytical model proposed by Logie et al. [27] was adopted to calculate the thermal stress.

First, the circumferential distribution of the inner and outer wall temperatures of the tube is fitted with a Fourier transform, where only the n = 1 term contributes to the thermal stress in the equation:

$$T_i = \overline{T_i} + \sum_{n=1}^{\infty} B_n^{'}\cos n\theta + D_n^{'}\sin n\theta \tag{11}$$

$$T_o = \overline{T_o} + \sum_{n=1}^{\infty} B_n^{''}\cos n\theta + D_n^{''}\sin n\theta \tag{12}$$

where $\overline{T_i}$ and $\overline{T_o}$ represent the average temperatures of the inner and

outer walls of the tube, respectively, and can be calculated using the following equations:

$$\overline{T_i} = \frac{1}{2\pi}\int_0^{2\pi} T_i d\theta \tag{13}$$

$$\overline{T_o} = \frac{1}{2\pi}\int_0^{2\pi} T_o d\theta \tag{14}$$

To calculate the axial thermal stress, it is necessary to define an expression for the circumferential temperature variation at different radii of the tube cross section:

$$T_\theta = T - (\overline{T_i} - \overline{T_o})\frac{ln\frac{R_o}{r}}{ln\frac{R_o}{R_i}} - \overline{T_o} \tag{15}$$

Assuming that the tube is restrained on both sides and there is no external mechanical load, the radial, circumferential, and axial thermal stresses can be calculated using the following equations:

$$\sigma_r = K\frac{\alpha E}{2(1-\nu)}\left[-ln\frac{R_o}{r} - \frac{R_i^2}{R_o^2 - R_i^2}\left(1 - \frac{R_o^2}{r^2}\right)ln\frac{R_o}{R_i}\right] + K_\theta\frac{\alpha E}{2(1-\nu)}\left(1 - \frac{R_i^2}{r^2}\right)\left(1 - \frac{R_o^2}{r^2}\right) \tag{16}$$

$$\sigma_\theta = K\frac{\alpha E}{2(1-\nu)}\left[1 - ln\frac{R_o}{r} - \frac{R_i^2}{R_o^2 - R_i^2}\left(1 + \frac{R_o^2}{r^2}\right)ln\frac{R_o}{R_i}\right] + K_\theta\frac{\alpha E}{2(1-\nu)}\left(3 - \frac{R_i^2 + R_o^2}{r^2} - \frac{R_i^2 r R_o^2}{r^4}\right) \tag{17}$$

$$\sigma_z = K\frac{\alpha E}{2(1-\nu)}\left[1 - 2ln\frac{R_o}{r} - \frac{2R_i^2}{R_o^2 - R_i^2}ln\frac{R_o}{R_i}\right] + K_\theta\frac{\alpha E\nu}{2(1-\nu)}\left(2 - \frac{R_i^2 + R_o^2}{r^2}\right) - \alpha E T_\theta \tag{18}$$

where $K$ and $K_\theta$ are the contributions of n = 0 term and n = 1 term, respectively to the thermal stress, which can be calculated using the following equation; where $B_1^{'}$, $D_1^{'}$, $B_1^{''}$, and $D_1^{''}$ are the coefficients in Eqs. (11) and (12).

$$K = \frac{\overline{T_i} - \overline{T_o}}{ln\frac{R_o}{R_i}} \tag{19}$$

$$K_\theta = \frac{rR_iR_o}{R_o^2 - R_i^2}\left[\left(\frac{B_1^{'}R_o - B_1^{''}R_i}{R_i^2 + R_o^2}\right)\cos\theta + \left(\frac{D_1^{'}R_o - D_1^{''}R_i}{R_i^2 + R_o^2}\right)\sin\theta\right] \tag{20}$$

Finally, according to the Von Mises theory of equivalent stress, the equivalent stress was calculated using the following equation:

$$\sigma_{eq} = \sqrt{\frac{(\sigma_r - \sigma_\theta)^2 + (\sigma_\theta - \sigma_z)^2 + (\sigma_z - \sigma_r)^2}{2}} \tag{21}$$

The structural and physical properties of the Inconel 625 alloy required for the calculations are listed in Table 4.

### 2.2. Model validation

An electromagnetic induction preheating receiver tube experiment was performed to validate the proposed model. The experimental system comprised three identical electromagnetic induction heaters and a receiver tube. Fig. 3 shows the schematic diagram of the experimental system, which displays the distribution of thermocouples on the surface of the receiver tube. Fig. 4 shows the diagram of electromagnetic induction heating receiver tube experiment system. Three identical electromagnetic induction heaters are placed on the side of the receiver tube. The heating power and heating time of the induction heaters are adjustable, and the initial distance between the receiver tube and the heaters is 10 mm. The receiver tube was made of Inconel 625 alloy with the exact dimensions shown in Fig. 2(b), and the outer wall of the tube has a Pyromark 2500 coating. The length of the test section of the receiver tube was 1 m, and each heater heated a 330 mm long tube. An electric heat-tracing device was installed on the surface of the tube to prevent the MS from solidifying during the salt circulation experiment. As shown in Fig. 3, to obtain the temperature distribution on the tube surface, K-type thermocouples with an accuracy of ±1 °C were welded at $\theta = 0°$, $\theta = 90°$, and $\theta = 180°$ in the middle section of each heater corresponding part of the tube. All thermocouples were connected to a computer through a data acquisition device. In addition, because the rear side of the receiver in tower CSP plants is typically insulated, the rear side of the receiver tube in this experimental system was installed with an insulation board made of aluminosilicate fiber cotton.

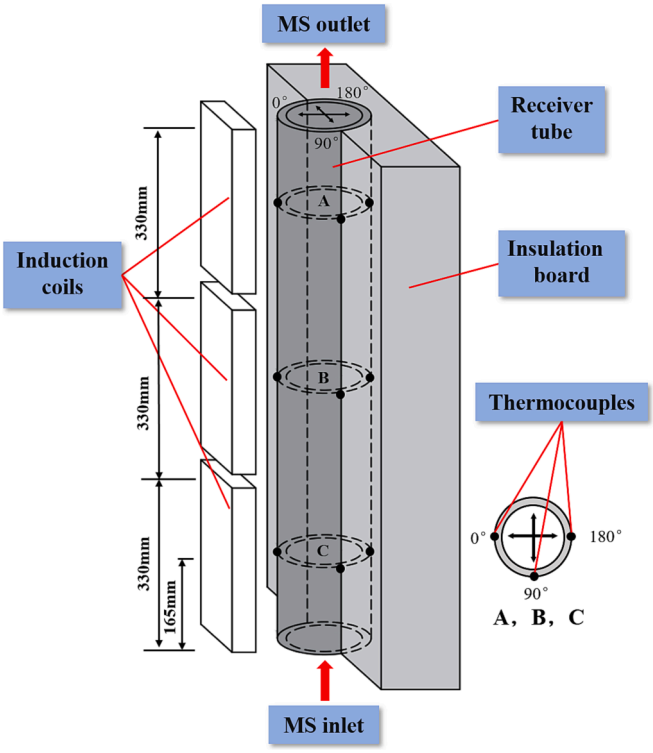


**Fig. 3.** Schematic diagram of test system and thermocouples distribution.

As the powers of the three heaters in the experiment were identical, the temperature data of the corresponding tube of one of the heaters were selected for comparison with the simulation results. Fig. 5 shows the temperature evolution at the points $\theta = 0°$, $\theta = 90°$, and $\theta = 180°$ in cross-section C when the coil power was 225 W, where the red and blue line indicate the experimental and simulation results, respectively. In general, the simulated and experimental results were relatively consistent, with maximum relative errors of 6.82, 3.15, and 4.25 % for the temperatures at three points, respectively. Notably, the temperature rise rate at the point $\theta = 0°$ in the experiment was greater than that in the simulation results in the 0–30 s period. This may attribute to the thermocouple welding point on the surface of the tube affecting the induction heating process, resulting in a faster temperature increase at this

**Table 4**
The structural physical properties of Inconel 625 alloy.

| Structural physical properties | Unit | Value |
|---|---|---|
| Young's modulus | GPa | 203 |
| Poisson's ratio | – | 0.3 |
| Linear thermal expansion coefficient | $K^{-1}$ | $12.25 \bullet 10^{-6}$ |

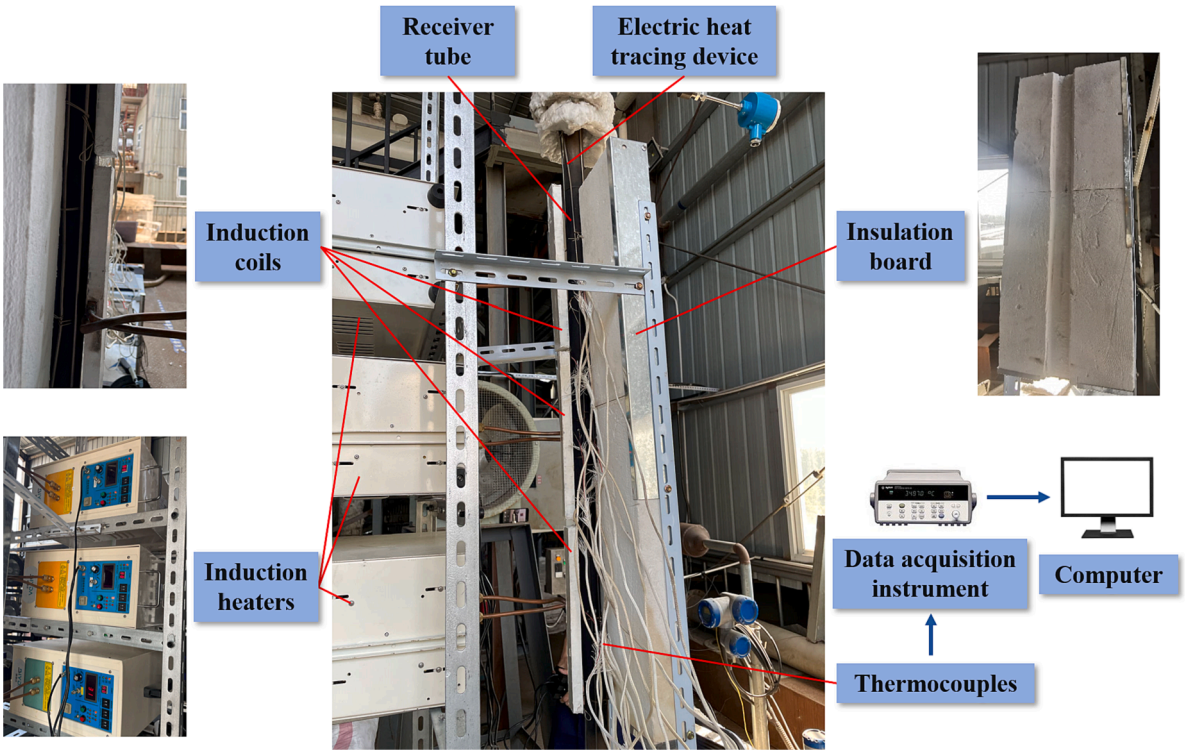


**Fig. 4.** Diagram of electromagnetic induction heating receiver tube experiment system.

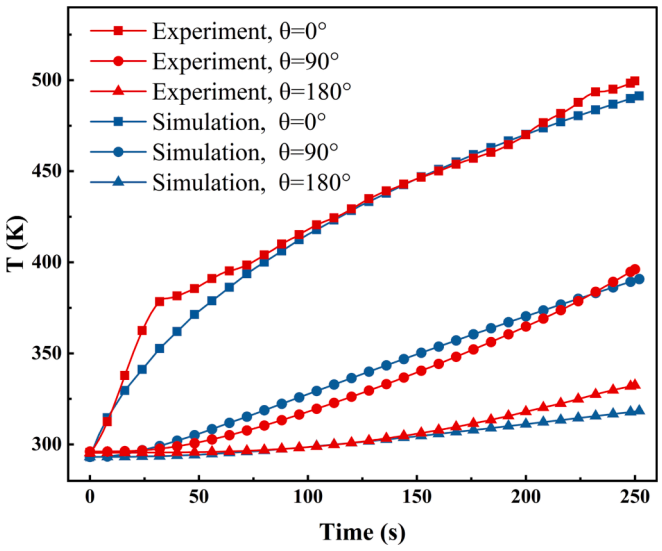


**Fig. 5.** Comparison of experimental results and simulation results.

point. This effect diminished with increase in the temperature. The temperature at the $\theta = 90°$ point in the experiment was lower than the simulation results in the period of 50–150 s, which may be attributed to the electric heat tracing device installed on the surface of the tube interferes with the experiment that causes the temperature at the $\theta = 90°$ point to rise more slowly. In the period of 200–250 s, the temperature rose at all three points in the experiment tended to become faster, which is probably owing to the deformation of the tube caused by the thermal stress in the experiment. Moreover, the distance between the tube and the heater becomes smaller, resulting in a faster heating rate. In general, the model depends on the receiver tube temperature.

## 3. Results and discussion

### 3.1. Preheating process

#### 3.1.1. Distribution of heat generation

Because the heat generated within the tube wall was uniformly distributed in the axial direction during preheating, a representative cross section of the tube at $z = 165$ mm was selected to analyze the heat generation and temperature distribution. Fig. 6 shows the heat generation distribution in the tube cross-section in case pre_1. As evident, the heat generation is primarily concentrated on the front side of the tube, that is, the side facing the induction heater. In the radial direction, heat generation was concentrated on the outer wall of the tube and rapidly decreased as the radius decreased. This is owing to the skin effect, which causes the induced current generated by the electromagnetic induction coil to concentrate on the outer surface of the tube; therefore, Joule heat is also concentrated there.

The effects of coil power $P$ and coil-to-tube distance $L$ on the heat generation distribution in the tube wall are shown in Figs. 7 and 8, respectively. These data were all exported from the COMSOL software. Fig. 7(a) shows the circumferential distribution of heat generation on the outer wall of the tube at different coil powers, and it is evident that the heat generation is concentrated in the range of $-60° \leq \theta \leq 60°$. In addition, because the heater is structured with two turns of coils placed side by side, the magnetic fields in the area between the coils are in opposite directions and partially cancel each other out; thus, the tube heat generation appears to exhibit two peaks, reaching a maximum at $\theta = 7.4°$ and $\theta = -7.4°$, while the heat generation at $\theta = 0°$ is slightly smaller. This contributed to a certain extent to the uniform distribution of heat generation and prevented excessive temperatures in certain areas of the tube during the heating process. When the coil power $P$ was 200, 300, 400, and 500 W, the maximum heat generation of the tube was 30.68, 46.00, 61.34, and 76.70 MW/m$^3$, respectively. As the coil power increased, the maximum heat generation in the tube increased. Fig. 7(b) shows the radial distribution of tube heat generation at $\theta = 0°$ for different coil powers. As evident, the heat generation was maximum at

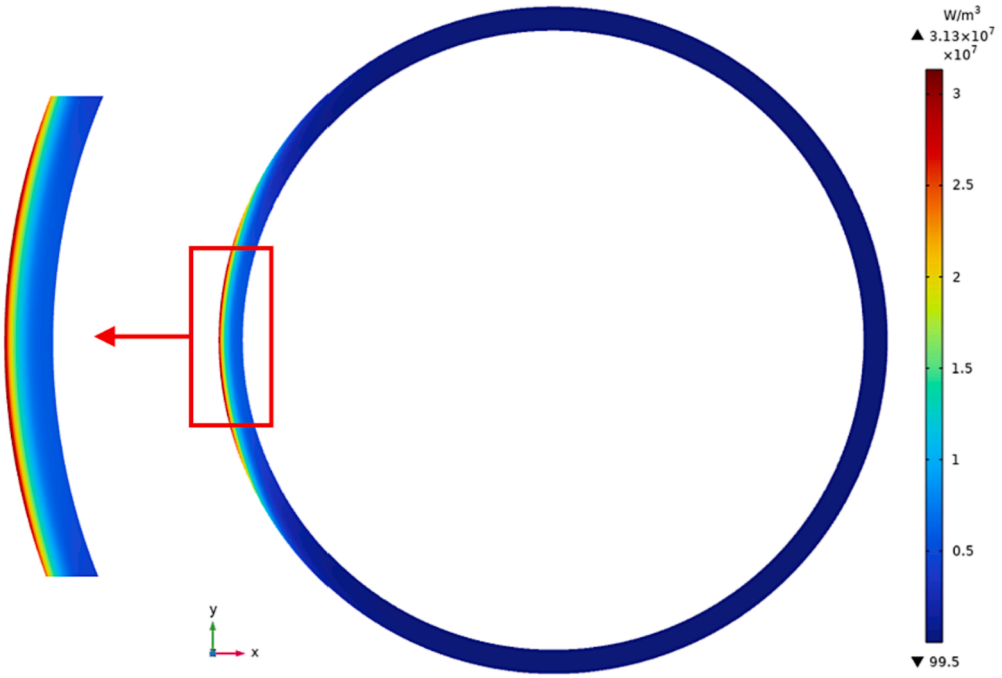


**Fig. 6.** Heat generation distribution of tube cross-section ($P$ = 200 W, $L$ = 10 mm).

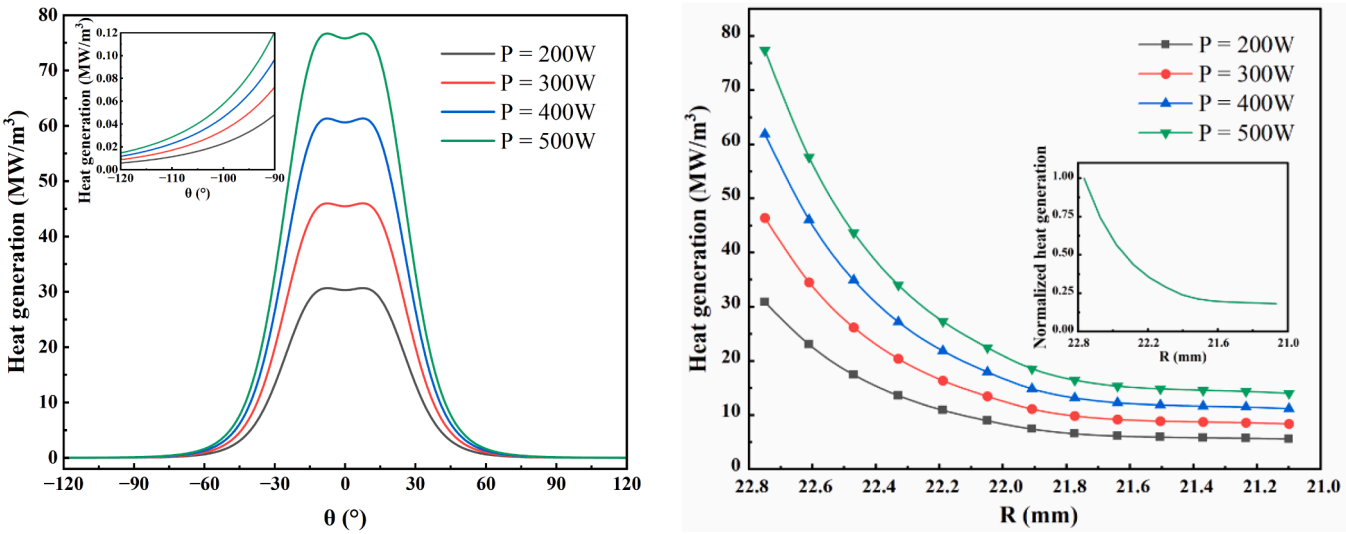


**Fig. 7.** Heat generation distribution at different coil powers ($L$ = 5 mm).

the outer wall and minimum at the inner wall and increased with increase in the coil power. Interestingly, after normalizing the four curves, they almost exactly overlapped, indicating that the relative distribution of the tube heat generation in the radial direction is independent of the coil power $P$.

Fig. 8(a) shows the circumferential distribution of the heat generation on the outer wall of the tube for different coil-to-tube distances. Overall, as the coil-to-tube distance increased, the tube heat generation decreased because the loss of magnetic field intensity increased. When $L$ = 15 mm and $L$ = 20 mm, the tube heat generation did not exhibit the two peaks mentioned above; however, when $L$ = 5 mm, the tube heat generation exhibited two obvious peaks at $\theta = 15.7^{\circ}$ and $\theta = -15.7^{\circ}$, while the tube heat generation at $\theta = 0^{\circ}$ was smaller. This indicated that the effect of the induction heater structure on the magnetic field distribution increased as $L$ decreased. When the coil-to-tube distance $L$ was 5, 10, 15, and 20 mm, the maximum heat generation of the tube was 38.01, 30.68, 29.61, and 26.24 MW/m$^3$, respectively. Fig. 8(b) shows the radial distribution of tube heat generation at $\theta = 0^{\circ}$ for different coil-to-tube distances. As evident, the radial distribution of the tube heat generation does not differ significantly for $L$ = 10 mm and $L$ = 15 mm, whereas for $L$ = 5 mm, the magnetic fields cancel each other out, resulting in a smaller tube heat generation. After normalizing the four curves, it was found that the tube heat generation was relatively large near the inner wall of the tube when $L$ = 5 mm, which was slightly different from the conclusion reached by Cano-Pleite et al. [18] because of the different structures of the two induction heaters.

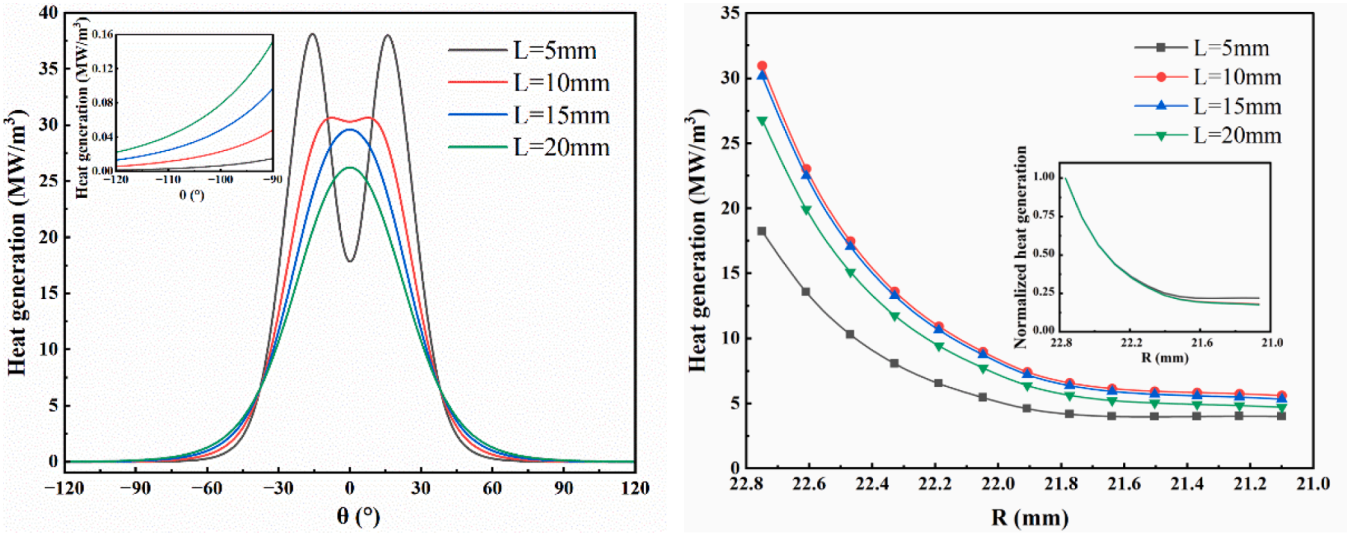


(a) Circumferential distribution (b) Radial distribution

**Fig. 8.** Heat generation distribution at different coil-to-tube distances ($P$ = 200 W).

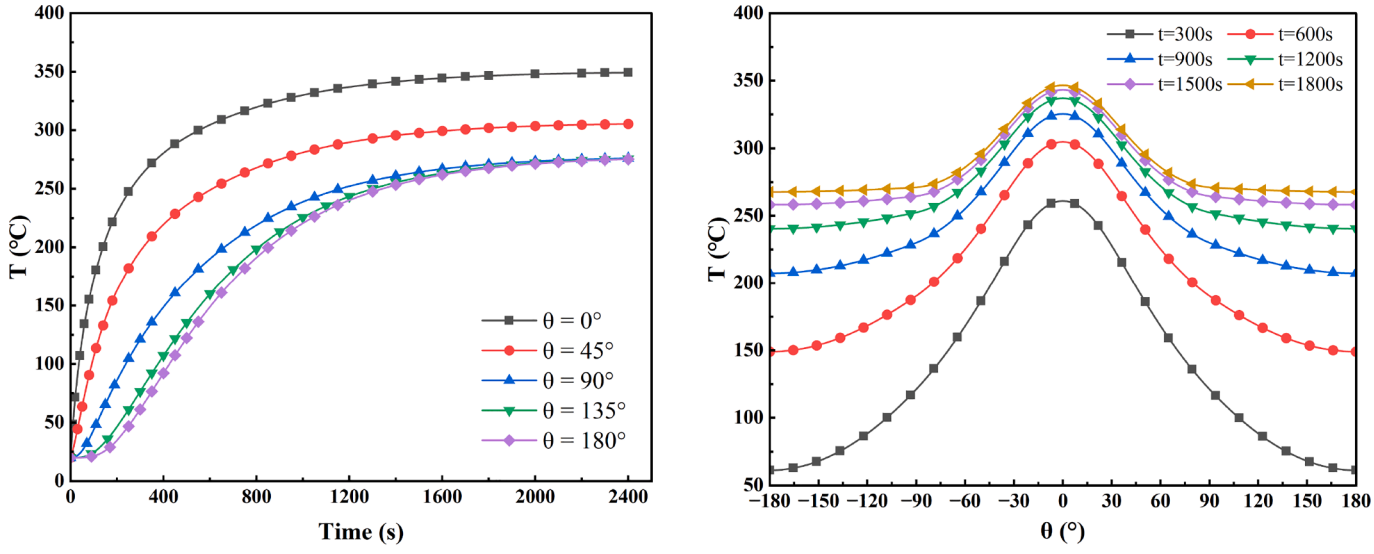


(a) Temperature evolution at different circumferential points (b) Evolution of the circumferential temperature distribution

**Fig. 9.** Temperature distribution and evolution of the outer wall of the tube ($P$ = 200 W, $L$ = 10 mm).

*3.1.2. Distribution and evolution of tube wall temperature*

The distribution and evolution of the tube wall temperature were focused upon the preheating process. In this study, $T_{max}$ and $T_{min}$ denote the maximum and minimum temperatures of the tube wall, respectively. Fig. 9 shows the temperature distribution and evolution of the outer wall of the tube for pre_1. As shown in Fig. 9(a), the temperature of the tube wall increased rapidly after preheating started. The heat generation was concentrated on the front side of the tube; therefore, the rate of temperature increase was significantly higher. In the preheating process, $T_{max}$ and $T_{min}$ occurred at $\theta = 0°$ and $\theta = 180°$, respectively. When the temperature of the tube was stable, the tube wall temperatures at $\theta = 0°$, $\theta = 45°$, $\theta = 90°$, $\theta = 135°$, and $\theta = 180°$ were 349.17, 305.33, 276.06, 275.55, and 275.28 °C, respectively. As shown in Fig. 9(b), the tube circumferential temperature gradient was larger in the early stage of the preheating process owing to the higher rate of temperature rise on the front side of the tube. At t = 300 s, the tube temperature difference was approximately 199.88 °C. When the temperature at the point $\theta = 0°$ gradually stabilized, heat was still continuously transferred to the back of the tube by conduction and radiation; thus, the tube circumferential temperature gradient gradually became smaller. When the temperature of the tube was stabilized, the tube temperature difference was approximately 73.89 °C. In addition, as the corresponding boundary condition at the back of the tube was set to be adiabatic, the temperature of the tube in the region of $\theta > 90°$ and $\theta < -90°$ was relatively uniform at approximately 267.75 °C when the tube temperature was stable.

The receiver of the tower CSP plant must be preheated within a short time. Otherwise, it affects the efficiency and economic return of the plant. Therefore, the rate of preheating is critical to the preheating process. The temperature of the receiver during the preheating process is typically limited to 230–350 °C to prevent thermal stress fatigue caused

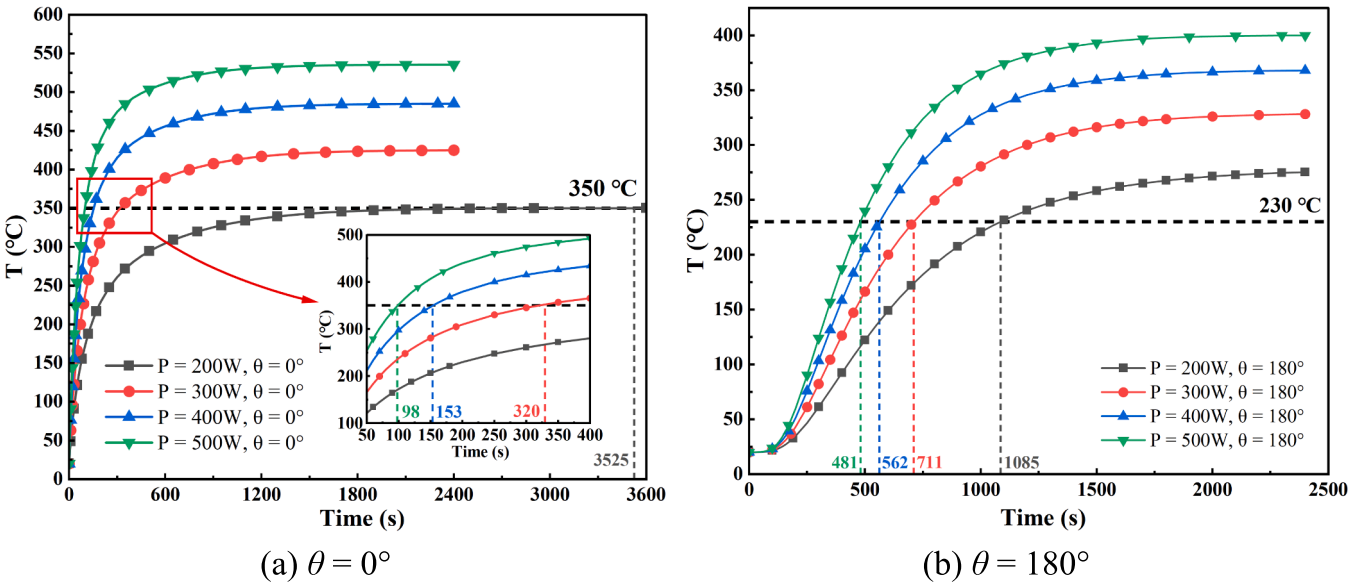


**Fig. 10.** Temperature evolution at points $\theta = 0°$ and $\theta = 180°$ at different coil powers ($L = 10$ mm).

by excessive temperature difference of the receiver tube [15]. In this study, $t_{230}$ denotes the time required for the lowest temperature of the tube (i.e., the temperature at $\theta = 180°$) to reach 230 °C, and $t_{350}$ denotes the time required for the highest temperature of the tube (i.e., the temperature at $\theta = 0°$) to reach 350 °C. Fig. 10 shows the temperature evolution at $\theta = 0°$ and $\theta = 180°$ on the outer wall of the tube for different coil powers, with the corresponding $t_{230}$ and $t_{350}$ indicated. In the cases of P = 300 W, P = 400 W, and P = 500 W, the simulation time was set to 2400 s because the temperature at the $\theta = 0°$ point exceeded 350 °C and stabilized. To ensure that the temperature at the $\theta = 0°$ point in the case of P = 200 W also reached 350 °C, the simulation time for this case was extended to 3600 s. From the figure, it is evident that the coil power $P$ exerted a more significant influence on the preheating time. The higher the coil power, the shorter the preheating time, and the higher the temperature at stabilization. When the coil power $P$ was 200, 300, 400, and 500 W, $t_{230}$ was 2400, 320, 153, and 98 s, and $t_{350}$ was 1085, 711, 562, and 481 s, respectively. Here, when $P = 200$ W, $t_{230}$ was less than $t_{350}$, which indicates that the tube was successfully preheated. In other cases, $t_{230}$ was greater than $t_{350}$, implying that before the $T_{min}$ reached 230 °C, its maximum temperature had exceeded 350 °C. Therefore, the position and orientation of the induction heater must be adjusted according to the tube temperature to successfully preheat the tube.

Fig. 11 shows the temperature evolution at $\theta = 0°$ and $\theta = 180°$ on the outer wall of the tube for different coil-to-tube distances as evident, the coil-to-tube distance exerts a minimal effect on the preheating process. In general, the larger $L$ is, the smaller the temperature rise rate of the tube, and the lower the temperature of the tube when it reaches a steady state. When $L = 5$ mm and $L = 10$ mm, the temperature change at the point of $\theta = 0°$ on the outer wall of the tube was almost the same, and the time to reach 350 °C was 3427 s and 3525 s, respectively, with a difference of 2.78 %. Moreover, when $L$ continued to increase, the energy loss increased, resulting in the $T_{max}$ remaining less than 350 °C when heating was stable. In Fig. 11(b), when the coil-to-tube distance $L$ was 5, 10, 15, and 20 mm, $t_{230}$ was 1049, 1085, 1181, and 1306 s, respectively, indicating that the effect of the coil-to-tube distance $L$ on the heating time was not apparent. In all four cases, $t_{230}$ was less than $t_{350}$, indicating that the tubes were successfully preheated.

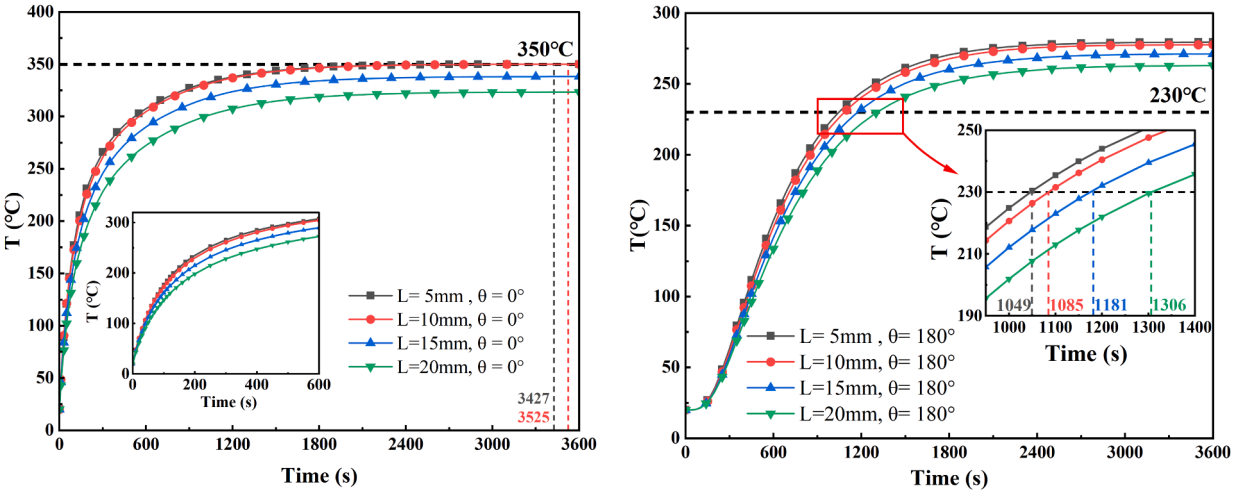


**Fig. 11.** Temperature evolution at points $\theta = 0°$ and $\theta = 180°$ at different coil-to-tube distances ($P = 200$ W).

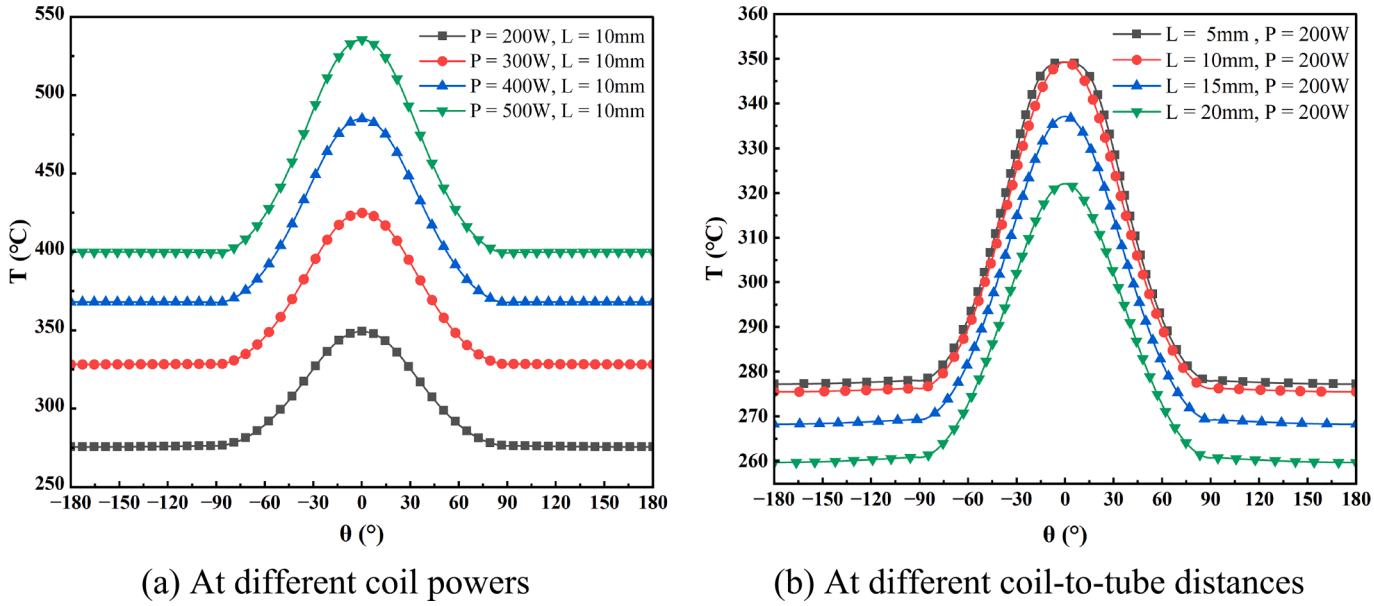


(a) At different coil powers (b) At different coil-to-tube distances

**Fig. 12.** Steady-state circumferential distribution of temperature at the outer wall of the tube for different parameters.

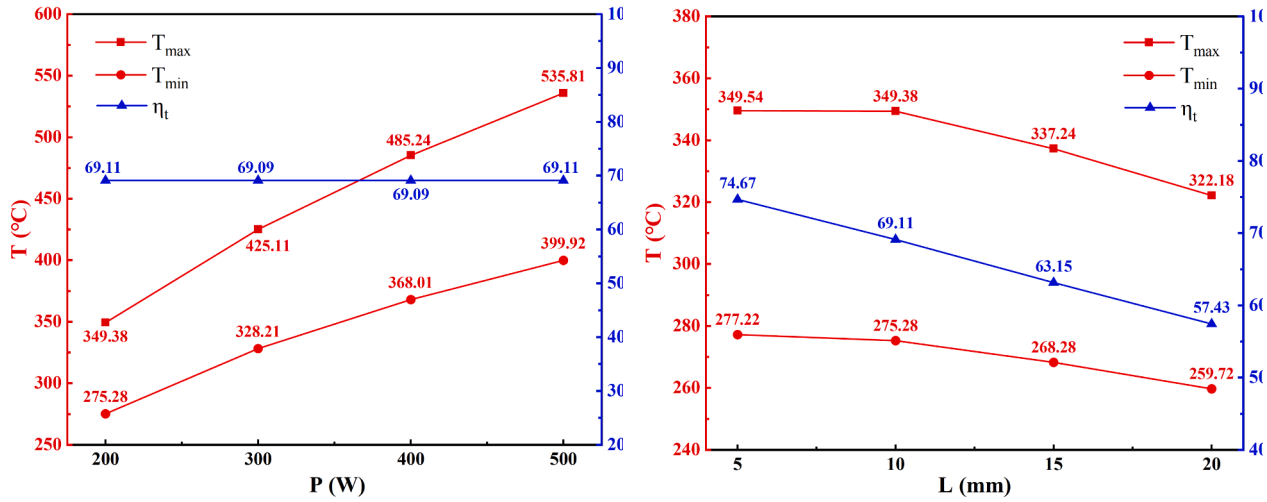


(a) At different coil powers (b) At different coil-to-tube distances

**Fig. 13.** $T_{max}$ and $T_{min}$ and heating efficiency $\eta_t$ at different parameters.

The tube wall temperature circumferential distribution at steady state for different coil powers and coil-to-tube distances is shown in Fig. 12. As evident, the coil power $P$ exerts a large effect on the tube temperature; the higher the $P$, the higher the tube temperature. Although the effect of the coil-to-tube distance $L$ on the tube temperature was relatively small, with an increase in $L$, the overall temperature of the tube slightly decreased. In addition, when $L = 5$ mm and $L = 10$ mm, the temperature distributions of the tubes were not significantly different; however, the temperature distribution of the former was relatively more uniform. Fig. 13 shows the effect of the coil power $P$ and the coil-to-tube distance $L$ on $T_{max}$ and $T_{min}$ and the heating efficiency $\eta_t$. The heating efficiency $\eta_t$ refers to the efficiency of the induction heater in heating the tube.

$$\eta_t = \frac{P_t}{P} \tag{22}$$

where $P_t$ is the total heat generation of the tube and $P$ is the coil power. As shown in Fig. 13(a), the tube temperature increased as the coil power $P$ increased, and the temperature difference increased. When the coil power $P$ was 200, 300, 400, and 500 W, the $T_{max}$ was 349.38, 425.11, 485.24, and 535.81 °C respectively, and the tube temperature difference was 74.10, 96.90, 117.23, and 135.89 °C, respectively. While the heating efficiency $\eta_t$ was not affected by the coil power $P$, the heating efficiency in all four cases was maintained at approximately 69.10 %. As shown in Fig. 13(b), when the coil-to-tube distance $L$ was greater than 10 mm, a larger $L$ resulted in lower $T_{max}$ and $T_{min}$. However, $T_{max}$ and $T_{min}$ were similar for $L = 5$ mm and $L = 10$ mm. In addition, the heating efficiency $\eta_t$ was greatly influenced by the coil-to-tube distance. When $L = 5$, 10, 15, and 20 mm, the heating efficiency $\eta_t$ was 74.67, 69.11, 63.15, and 57.43 %, respectively. In addition, although the $T_{max}$ and $T_{min}$ were similar for $L = 5$ mm and $L = 10$ mm, the heating efficiency $\eta_t$ of the former was 5.56 % higher than that of the latter, which indicates that the average temperature of the tube was higher and the temperature distribution was more uniform for $L = 5$ mm.

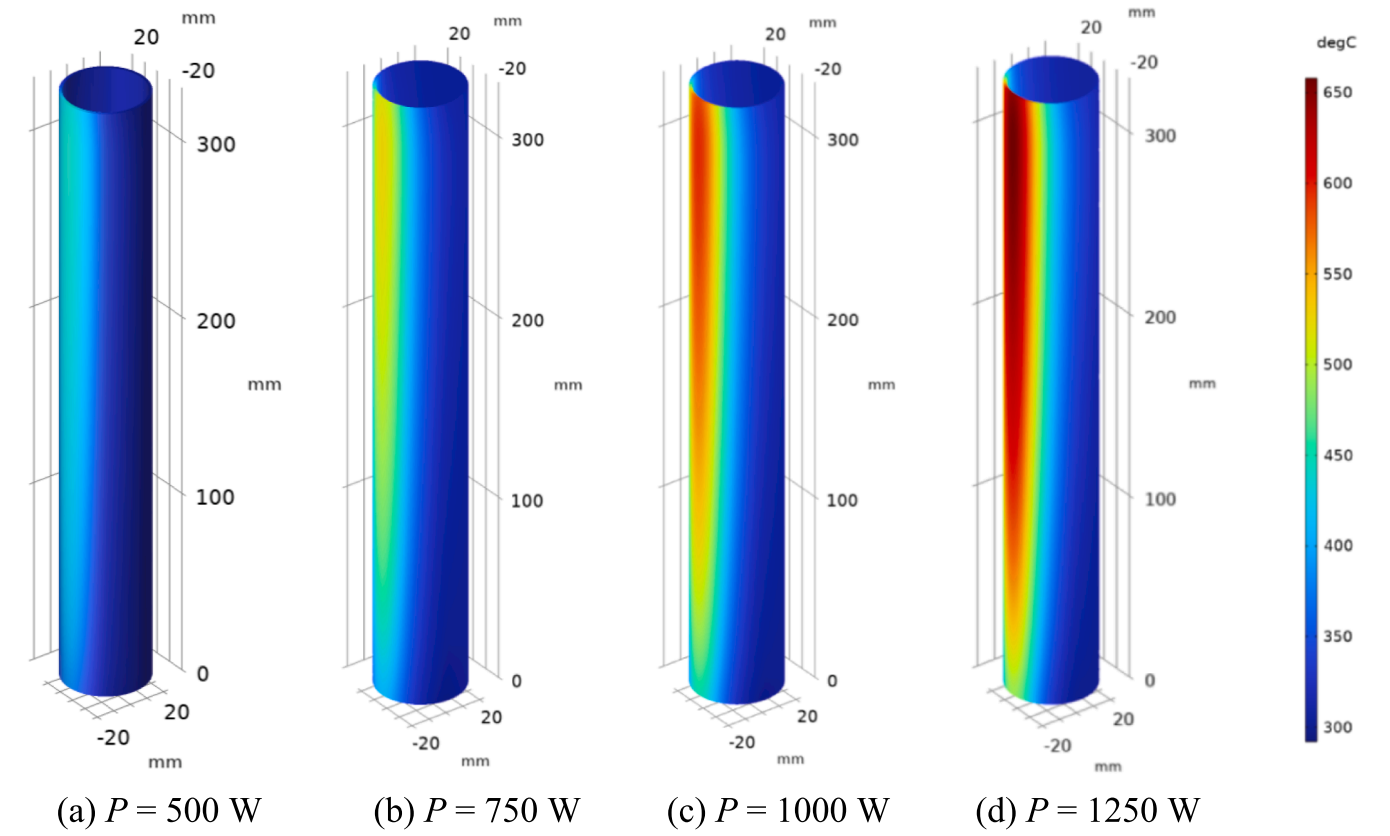


**Fig. 14.** Temperature distribution of tube wall at different coil powers.

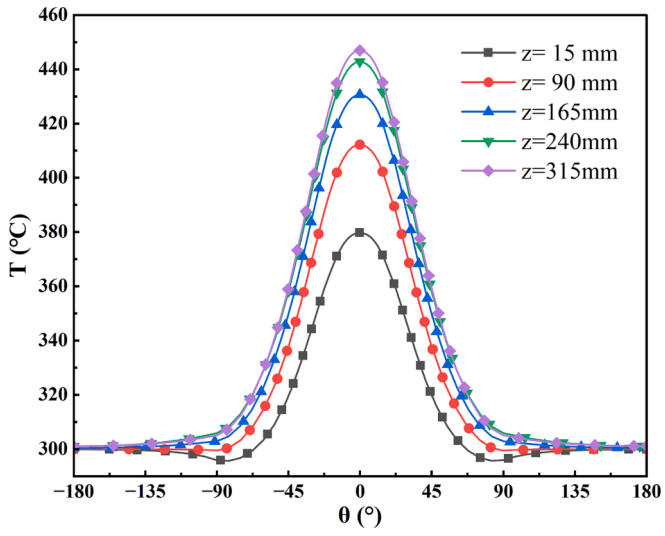


**Fig. 15.** Tube wall circumferential temperature distribution.

### 3.2. Salt circulating condition

#### 3.2.1. Distribution of tube wall temperature

Fig. 14 shows the tube wall temperature distributions at different coil powers under salt circulation conditions. The tube temperature was not uniform in the axial direction because the MS temperature gradually increased. Fig. 15 shows the tube wall circumferential temperature distribution for different cross sections in the case of salt_1. To prevent the boundary conditions on the upper and lower surfaces of the model from influencing the results, a section with $z$ = 15 mm was selected as the initial section, and a section was acquired every 75 mm for the analysis. As evident from the figure, the temperature at the front of the tube wall gradually became higher along the axial direction, and the maximum temperature of the tube section increased from 379.73 °C at $z$ = 15 mm to 446.94 °C at $z$ = 315 mm (increase of 17.71 %). In addition, because the rear of the tube was set to be adiabatic, and the MS near the back of the tube was not heated for the time being, the temperature at the back of the tube did not change significantly and remained approximately 300 °C, which is also the inlet temperature of the MS. Consequently, the tube temperature difference became progressively larger along the axial direction.

The heat loss of a receiver significantly affects its efficiency and is closely related to the temperature of the tube wall. Radiant heat dissipation is a major part of the heat loss in receivers compared to convective heat loss [10]. Fig. 16 shows the effects of the coil-to-tube distance $L$, coil power $P$, MS inlet temperature $T_{s,in}$, MS inlet velocity $v_{s,in}$ and ambient temperature $T_{amb}$ on the $T_{max}$, average temperature of the tube wall, and radiation heat loss. As shown in the figure, in general, radiant heat dissipation is positively correlated with the temperature of the tube. The coil-to-tube distance $L$ had a minimal effect on the tube wall temperature or radiation heat loss. As $L$ increased from 5 to 20 mm, the average wall temperature and radiation heat loss power decreased by 1.36 and 6.82 %, respectively. However, $T_{max}$ at $L$ = 5 mm was lower than that at $L$ = 10 mm, which further indicated that the tube wall temperature distribution was relatively more uniform at $L$ = 5 mm. The coil power $P$, MS inlet temperature $T_{s,in}$, and MS inlet velocity $v_{s,in}$ greatly affected the tube wall temperature and radiation heat loss. When the coil power $P$ increased from 500 to 1250 W, the $T_{max}$ increased from 448.47 to 657.93 °C; when the MS inlet temperature $T_{s,in}$ increased from 250 to 400 °C, the $T_{max}$ increased from 417.31 to 507.29 °C; when the MS inlet velocity $v_{s,in}$ increased from 0.1 to 0.4 m/s, the $T_{max}$ decreased from 448.47 to 381.16 °C. However, the ambient temperature $T_{amb}$ had almost no effect on the tube temperature, although an increase in $T_{amb}$

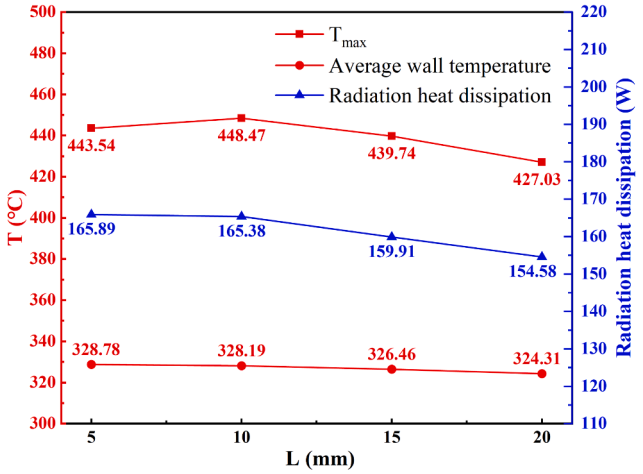


(a) Different coil-to-tube distances

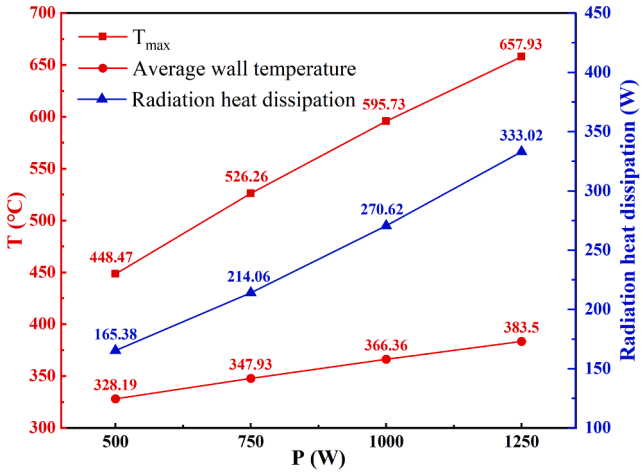


(b) Different coil powers

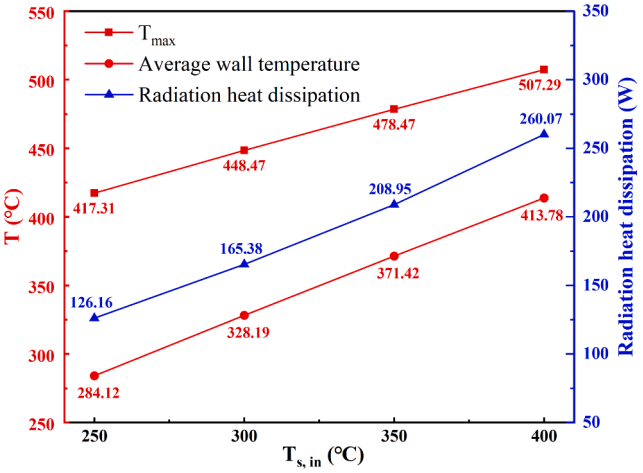


(c) Different MS inlet temperatures

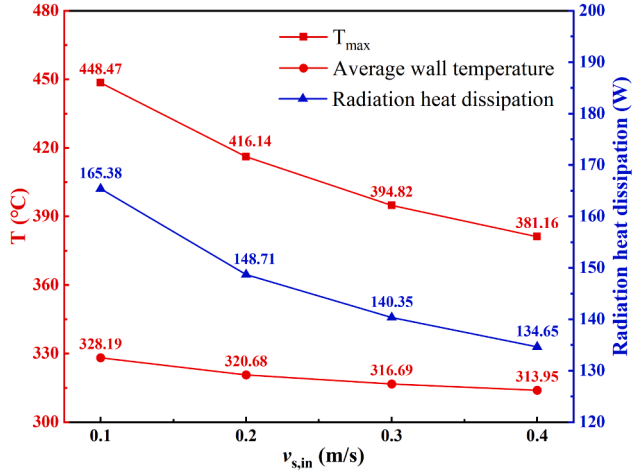


(d) Different MS inlet velocities

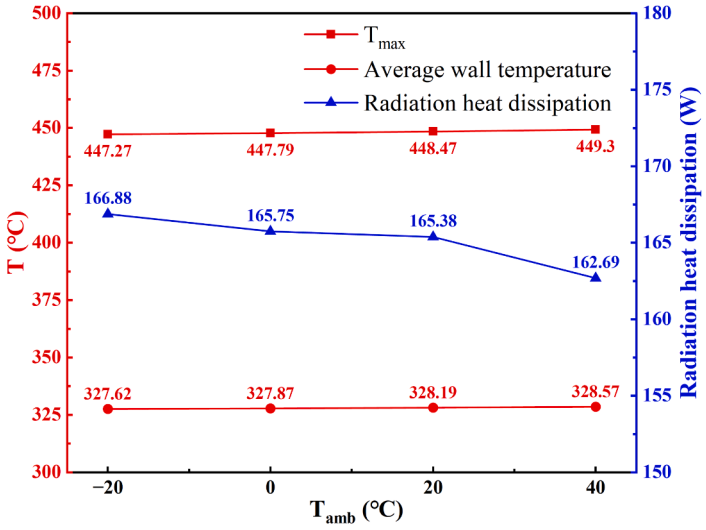


(e) Different ambient temperatures

**Fig. 16.** Effect of different parameters on tube temperature and radiant heat dissipation.

slightly reduced the radiant heat dissipation from the tube. As $T_{amb}$ increased from −20 to 40 °C, the radiant heat dissipation power decreased by 2.51 %. Notably, excessive tube wall temperature may damage the receiver tube and may cause the internal Solar Salt temperature to exceed 600 °C. This causes the Solar Salt to decompose into nitrogen oxide gas, thereby increasing the pressure inside the tube, which is a safety hazard. Therefore, during receiver operation, if the solar radiation intensity is excessively high, the maximum tube temperature can be appropriately reduced by increasing the mass flow rate of the MS.

### 3.2.2. MS temperature and heating efficiency

The purpose of a receiver is to receive solar radiation and transfer heat to the MS; therefore, the distribution and evolution of the temperature of the MS are among the most important aspects in the study of receivers. Fig. 17 shows the MS temperature distribution in the cross section of the tube at $z = 165$ mm for different coil powers. It is evident that there is an obvious temperature gradient of MS. The MS in the area near the front of the tube had a higher temperature owing to the heating effect of the wall, whereas that in the area near the rear of the tube maintained a temperature of approximately 300 °C in line with the $T_{s,in}$ because the heat was not been transferred here yet. In addition, only a small fraction of the MS in the cross-section was heated by the wall because the heat generated within the tube wall was excessively concentrated at the front of the tube, resulting in a higher wall temperature.

The temperature increase in the MS and efficiency of heating the MS are the criteria for directly judging the thermal performance of a receiver. Fig. 18 shows the effect of different parameters on the temperature rise $\Delta T$ and heating efficiency $\eta_s$ of the MS, where the efficiency $\eta_s$ is calculated using the following equation:

$$\eta_s = \frac{C_p \rho \pi R_i^2 v_{s,in} \Delta T}{P} \tag{23}$$

where $C_p$ is the specific heat of the MS, $\rho$ is the density of the MS, $R_i$ is the inner radius of the tube, $v_{s,in}$ is the inlet velocity of the MS, $\Delta T = T_{s,out}$, $T_{s,in}$, $T_{s,out}$ is the outlet temperature of the MS, $T_{s,in}$ is the inlet temperature of the MS, and $P$ is the coil power. As evident from the figure, the MS temperature rises $\Delta T$, and the heating efficiency $\eta_s$ followed the same trend in all cases except for the case of changing the MS inlet velocity, which can also be derived from the formula for the efficiency. The coil-to-tube distance $L$, coil power $P$, MS inlet temperature $T_{s,in}$, and MS inlet velocity $v_{s,in}$ had a significant effect on $\Delta T$ and $\eta_s$. When $L$ increased from 5 to 20 mm, $\Delta T$ and $\eta_s$ decreased by 0.078 °C and 6.34 %, respectively. When $P$ increased from 500 to 1250 W, $\Delta T$ and $\eta_s$ increased by 0.954 °C and 7.21 %, respectively. Further, when $T_{s,in}$ increased from 250 to 400 °C, $\Delta T$ and $\eta_s$ decreased by 0.346 °C and 28.35 %, respectively, because the temperature difference between the tube wall and the MS decreased; therefore, the convective heat transfer rate and heating efficiency decreased. When $v_{s,in}$ increased from 0.1 to 0.4 m/s, $\Delta T$ decreased by 0.341 °C; however, $\eta_s$ increased by 7.87 %. This is because the MS stayed in the tube for less time and was heated for less time, thus, $\Delta T$ decreased. Whereas, the convective heat transfer coefficient increased, this $\eta_s$ increased. However, $T_{amb}$ exerted a relatively small effect on $\Delta T$ and $\eta_s$, which mainly affected the radiation heat dissipation of the tube. As $T_{amb}$ increased from −20 to 40 °C, the MS temperature increased slightly by 0.017 °C, and the heating efficiency increased slightly by 0.07 % owing to the reduced radiation heat loss from the tube.

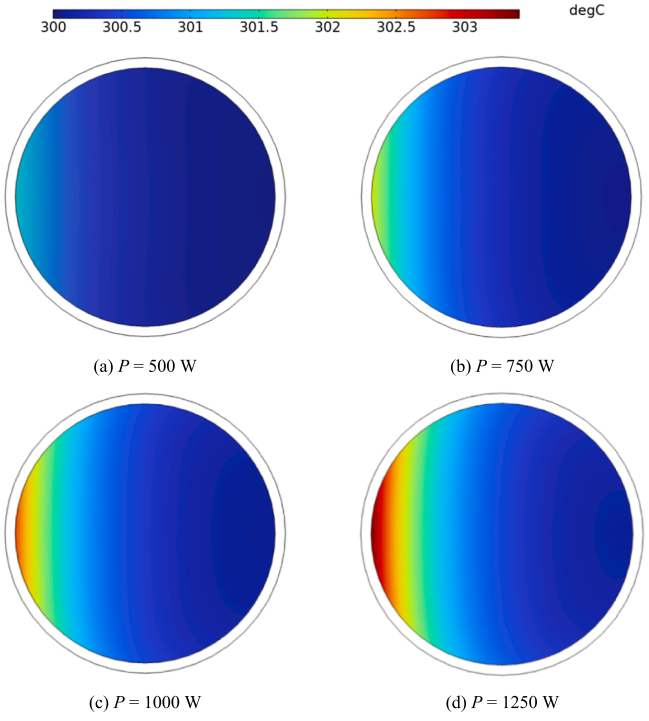


**Fig. 17.** MS temperature distribution under different coil powers.

### 3.3. Thermal stress

Highly nonuniform heat flow can cause a nonuniform temperature distribution on the wall of the tube, which can result in a large thermal stress, which is an important concern for tower CSP plants. In this section, the tube thermal stress evolution and distribution are studied for coil power $P = 500$ W and coil-to-tube distance $L = 10$ mm. Fig. 19 shows the evolution of thermal stress during the preheating process. As evident from Fig. 19(a) the radial and circumferential thermal stresses were small and almost negligible compared to the axial thermal stress, and the axial thermal stress primarily determined the magnitude of $\sigma_{eq}$. Fig. 19(b) shows that the $\sigma_{eq}$ at each point of the receiver tube increased, then decreased during the preheating process, and finally stabilized. This is because the circumferential temperature gradient of the tube gradually increased during the preheating period and then slowly decreased until it stabilized. The maximum $\sigma_{eq}$ of the tube was reached at $\theta = 0°$ at t = 170 s, which was 551.72 MPa. When the preheat is stable, $\sigma_{eq}$ is maximum at $\theta = 0°$ and minimum at $\theta = 45°$, which were 247.74 and 42.26 MPa, respectively.

Fig. 20 shows the circumferential distribution of $\sigma_{eq}$ for each tube section under the salt circulation conditions. The results indicate that the maximum tube $\sigma_{eq}$ occurred at $\theta = 0°$ and decreased rapidly as $\theta$ increased. The minimum $\sigma_{eq}$ was observed at $\theta = 45°$, followed by a slow increase. On the rear side of the tube, $\sigma_{eq}$ tended to stabilize. In addition, the tube thermal stress progressively increased along the MS flow direction with the continuous increase in the circumferential temperature difference in the tube (Fig. 15). The maximum $\sigma_{eq}$ increased from 154.51 to 254.34 MPa for the section with $z = 15$ mm compared to the section with $z = 315$ mm. Fig. 21 shows the $\sigma_{eq}$ and temperature circumferential distributions for a cross-section of the tube, $z = 165$ mm, under preheat stabilization and salt circulation conditions. It is evident that the $\sigma_{eq}$ of the tube at preheat stabilization was slightly larger than that of the salt circulation condition; however, they are nearly the same, with the maximum $\sigma_{eq}$ of 247.74 and 236.69 MPa, respectively (difference of only 4.46 %). This can be explained by the fact that the circumferential temperature gradient of the tube was very similar, despite the large difference in the temperature of the tube in both cases, as shown in Fig. 21 (b). This also indicates that the tube thermal stress is closely related to the circumferential temperature gradient.

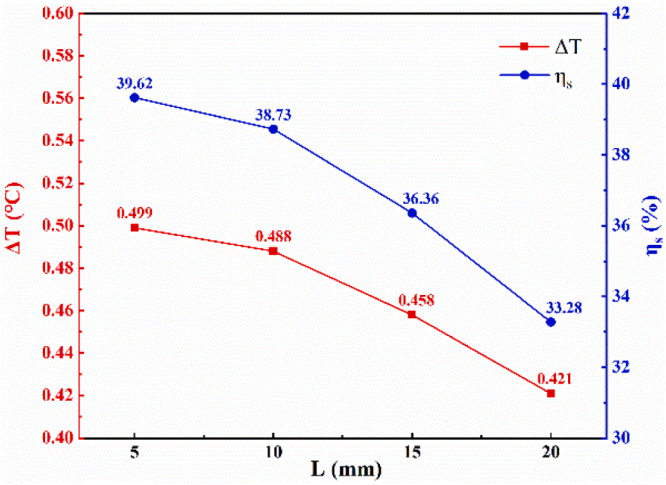


(a) Different coil-to-tube distances

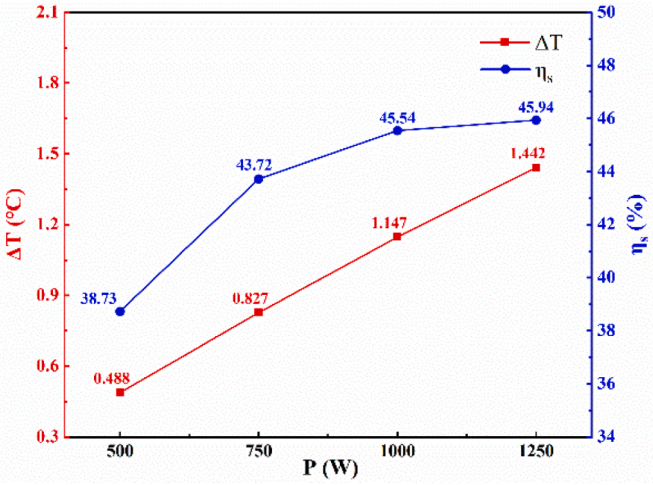


(b) Different coil powers

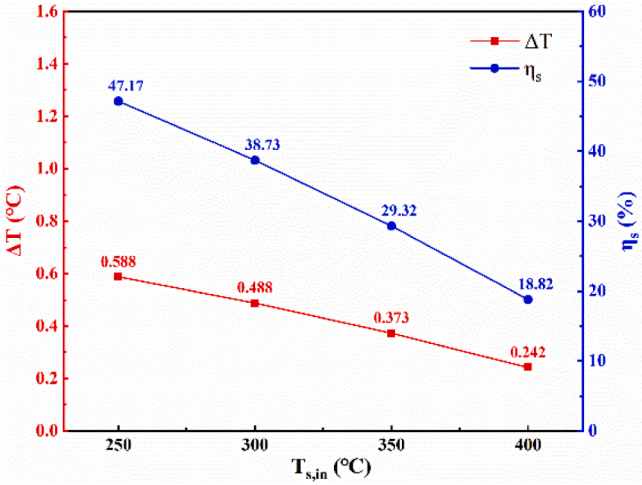


(c) Different MS inlet temperatures

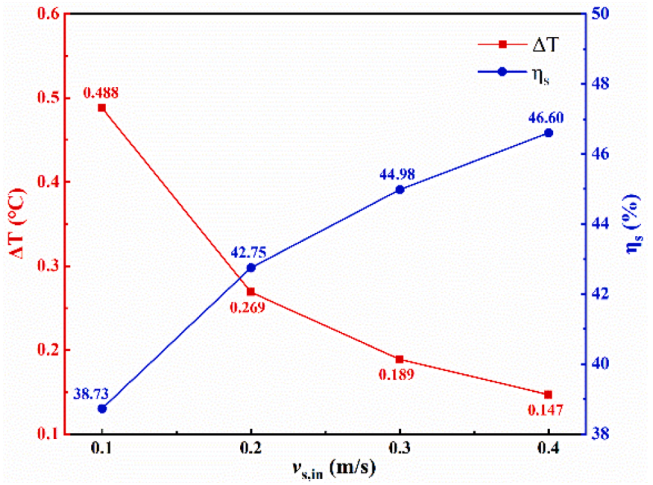


(d) Different MS inlet velocities

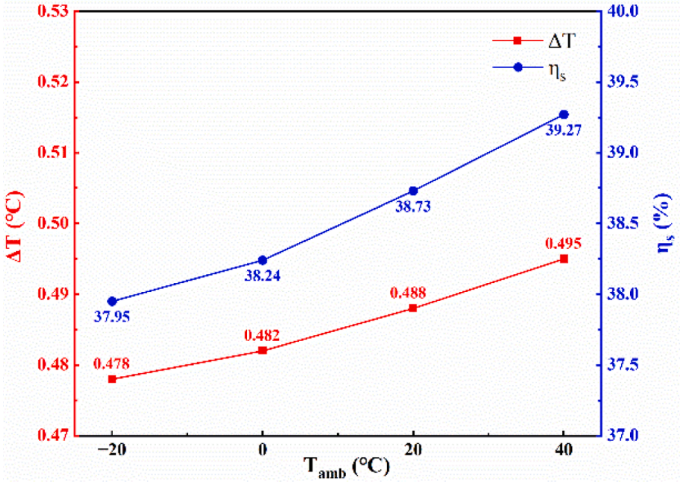


(e) Different ambient temperatures

**Fig. 18.** Effect of different parameters on the temperature rise $\Delta T$ and heating efficiency $\eta_s$ of the MS.

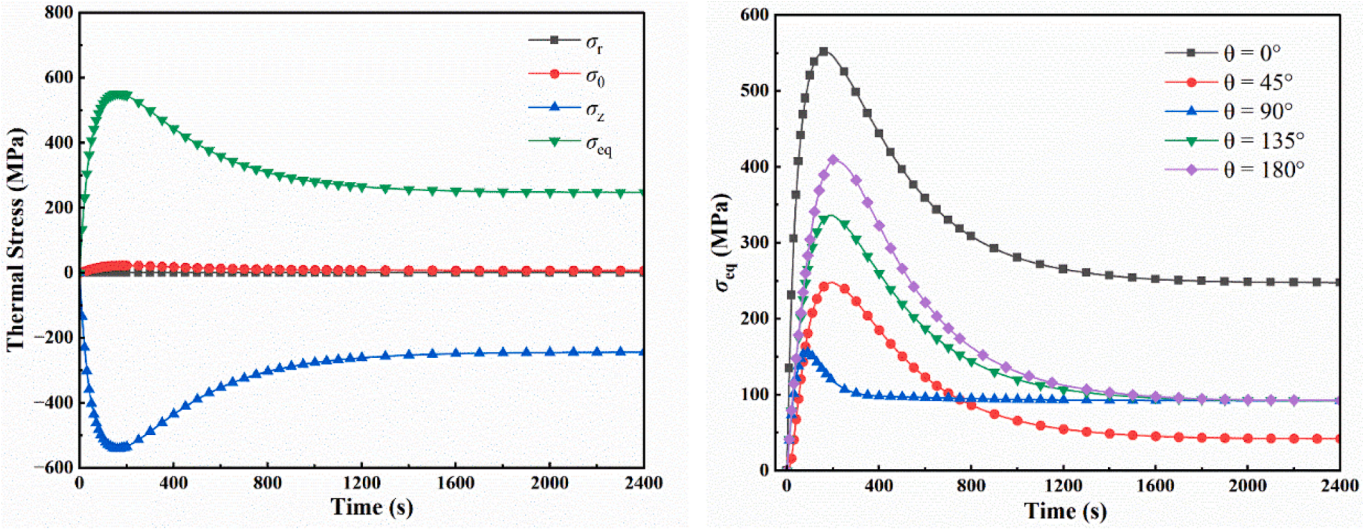


(a) Evolution of thermal stress at the point $\theta$=0°

(b) Evolution of $\sigma_{eq}$ at different circumferential points

**Fig. 19.** Evolution of thermal stress in the tube during preheating.

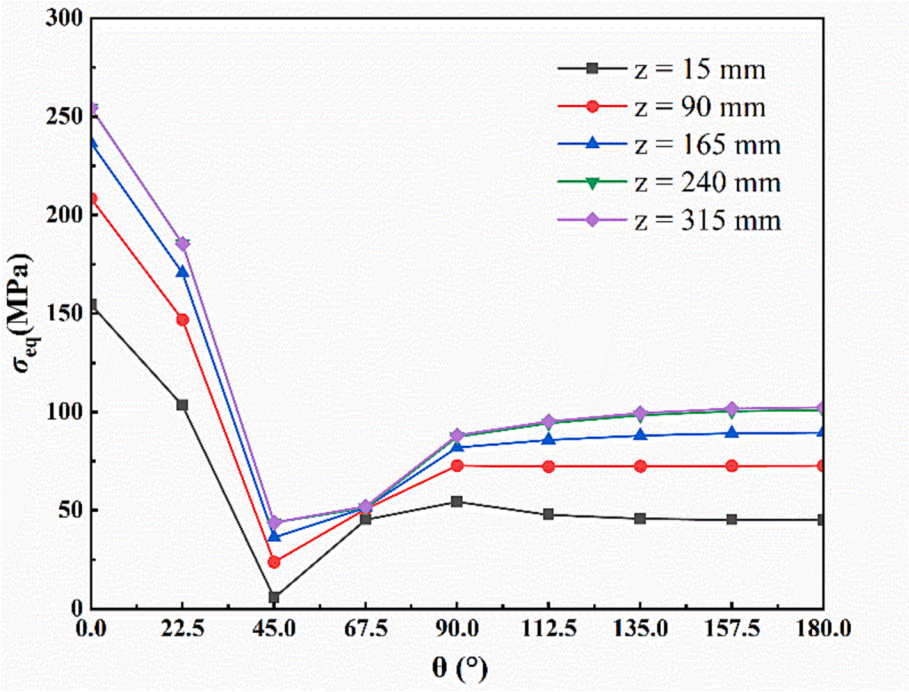


**Fig. 20.** Circumferential distribution of $\sigma_{eq}$ for each section of the tube.

## 4. Conclusion

In this study, a 3D model that couples electromagnetic induction, heat transfer, and turbulence, was developed to investigate the effects of key parameters on the induction heating process of the receiver. Experiments are conducted to verify the reliability of the proposed model. The following conclusions were drawn.

(1) The coil power P and coil-to-tube distance L strongly influenced the tube heat generation. As P increased from 200 to 500 W and L increased from 5 to 20 mm, the maximum heat generation of the tube increased by 149.98 % and decreased by 30.97 %, respectively. Owing to the skin effect, heat generation was concentrated on the outer surface of the tube. In addition, the unique structure of the induction heater resulted in two heat generation peaks on the outer surface of the tube.

(2) During preheating, the rate of temperature increase at the rear of the tube was significantly lower than that at the front. An increase in *P* significantly accelerated the preheating process. As *P*

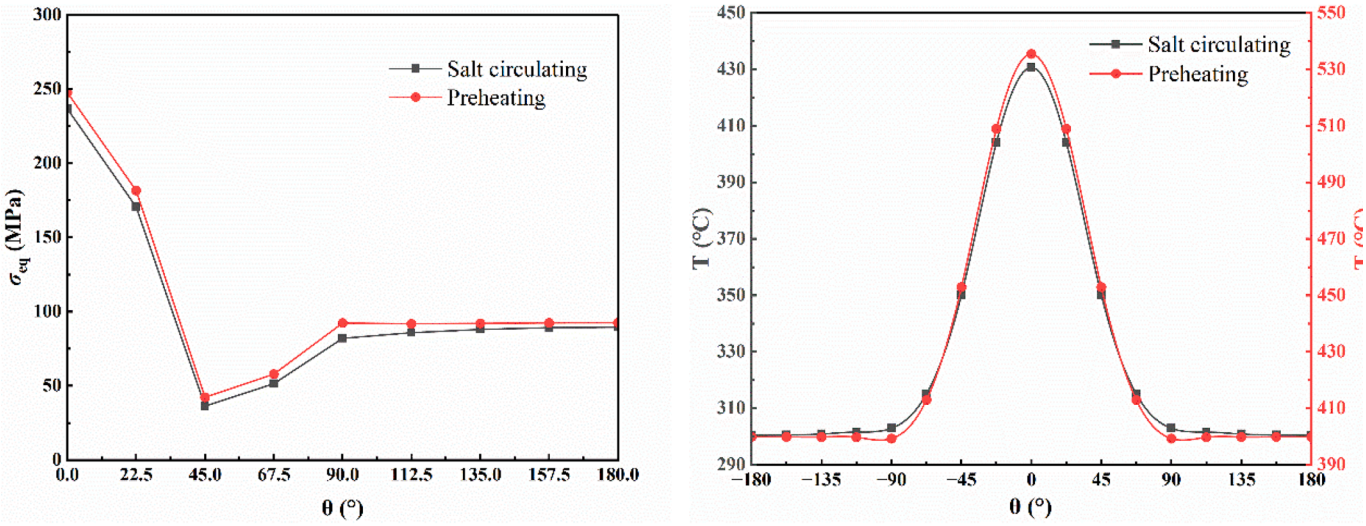


(a) Circumferential distribution of $\sigma_{eq}$ (b) Circumferential distribution of temperature

**Fig. 21.** Circumferential distribution of tube $\sigma_{eq}$ and temperature at preheat stabilization and salt circulating conditions.

increased from 200 to 500 W, $t_{350}$ and $t_{230}$ decreased by 95.96 and 55.67 %, respectively.

(3) When the MS circulated in the tube, the temperature at the front side of the tube wall gradually increased along the axial direction, whereas that at the rear side of the tube did not change significantly and remained approximately $T_{s,in}$. The heating efficiency $\eta_s$ increased as the coil power $P$, MS inlet velocity $v_{s,in}$ and ambient temperature $T_{amb}$ increased. Among them, $T_{s,in}$ had the greatest effect on the efficiency. As the $T_{s,in}$ increased from 250 to 400 °C, $\eta_s$ decreased by 28.35 %.

(4) Among the three directions of thermal stress, $\sigma_z$ mainly determined the $\sigma_{eq}$ of the receiver. During preheating, the $\sigma_{eq,max}$ of the receiver reached 551.72 MPa. When the temperature was stabilized, the $\sigma_{eq,max}$ and $\sigma_{eq,min}$ were reached at $\theta = 0°$ and $\theta = 45°$ points, respectively. Under the salt-circulating condition, $\sigma_{eq}$ increased along the axial direction because the tube circumferential temperature gradient also increased. The $\sigma_{eq}$ of the tube under preheat stabilization was slightly larger than that under salt circulating condition, with a difference of only 4.46 %.

## Declaration of Competing Interest

The authors declare that they have no known competing financial interests or personal relationships that could have appeared to influence the work reported in this paper.

## Data availability

Data will be made available on request.

## Acknowledgement

This work was supported by the Fundamental Research Funds for the Central Universities (2022ZFJH004).

## References

[1] L. Juan, Y. Shen, X. Li, A. Hasnaoui, BRICS carbon neutrality target: Measuring the impact of electricity production from renewable energy sources and globalization, J. Environ. Manage. 298 (2021), 113460.
[2] B. Wan, L. Tian, M. Fu, G. Zhang, Green development growth momentum under carbon neutrality scenario, J. Clean. Prod. 316 (2021), 128327.
[3] A. Peinado Gonzalo, A. Pliego Marugán, F.P. García Márquez, A review of the application performances of concentrated solar power systems, Appl. Energy 255 (2019), 113893.
[4] A. Bonk, S. Sau, N. Uranga, M. Hernaiz, T. Bauer, Advanced heat transfer fluids for direct molten salt line-focusing CSP plants, Prog. Energy Combust. Sci. 67 (2018) 69–87.
[5] M. Imran Khan, F. Asfand, S.G. Al-Ghamdi, Progress in research and technological advancements of commercial concentrated solar thermal power plants, Sol. Energy 249 (2023) 183–226.
[6] Y. He, Y. Qiu, K. Wang, F. Yuan, W. Wang, M. Li, J. Guo, Perspective of concentrating solar power, Energy 198 (2020), 117373.
[7] M. Slootweg, K.J. Craig, J.P. Meyer, A computational approach to simulate the optical and thermal performance of a novel complex geometry solar tower molten salt cavity receiver, Sol. Energy 187 (2019) 13–29.
[8] Q. Yu, P. Fu, Y. Yang, J. Qiao, Z. Wang, Q. Zhang, Modeling and parametric study of molten salt receiver of concentrating solar power tower plant, Energy 200 (2020), 117505.
[9] M.A. Qaisrani, J. Fang, Y. Jin, Z. Wan, N. Tu, M. Khalid, M.U. Rahman, J. Wei, Thermal losses evaluation of an external rectangular receiver in a windy environment, Sol. Energy 184 (2019) 281–291.
[10] M.A. Qaisrani, J. Wei, J. Fang, Y. Jin, Z. Wan, M. Khalid, Heat losses and thermal stresses of an external cylindrical water/steam solar tower receiver, Appl. Therm. Eng. 163 (2019), 114241.
[11] B.S. Emerick, F.G. Battisti, A.K. Da Silva, Geometric optimization of a solar tower receiver operating with supercritical CO2 as working fluid, Appl. Therm. Eng. 228 (2023), 120318.
[12] D.J. Erasmus, A. Sánchez-González, M. Lubkoll, K.J. Craig, T.W. von Backström, Thermal performance characteristics of a tessellated-impinging central receiver, Appl. Therm. Eng. 229 (2023), 120529.
[13] B. Du, Y. He, Z. Zheng, Z. Cheng, Analysis of thermal stress and fatigue fracture for the solar tower molten salt receiver, Appl. Therm. Eng. 99 (2016) 741–750.
[14] K. Peng, F.G.F. Qin, R. Jiang, Effect of tube size on the thermal stress in concentrating solar receiver tubes, J. Sol. Energy Eng. 142 (2020).
[15] Y. Zuo, Y. Li, H. Zhou, Numerical study on preheating process of molten salt tower receiver in windy conditions, Energy 251 (2022), 123893.
[16] R. Pérez-Álvarez, C. Marugán-Cruz, D. Santana, A. Acosta-Iborra, Influence of eccentricity on the thermomechanical performance of a bayonet tube of a central solar receiver, Appl. Therm. Eng. 223 (2023), 119988.
[17] R. Pérez-Álvarez, E. Cano-Pleite, D. Santana, A. Acosta-Iborra, Impact of a mechanical attachment on the preheating temperatures of a central receiver tube, Appl. Therm. Eng. 215 (2022), 118854.
[18] E. Cano-Pleite, M. Fernández-Torrijos, D. Santana, A. Acosta-Iborra, Heat generation depth and temperature distribution in solar receiver tubes subjected to induction, Appl. Therm. Eng. 204 (2022), 117902.
[19] S.W. Wang, C. Zhou, C.X. Cai, H.H. Zhu, N.X. Wang, Y. Zou, Experimental research on convective heat transfer characteristics of molten salt in a pebble bed channel with internal heat source, Nucl. Eng. Des. 387 (2022), 111619.
[20] C. Zhang, Y. Wu, Y. Lu, Experimental and numerical study on induction heating performance of quaternary nitrate-nitrite molten salt, Int. J. Energy Res. 45 (2021) 2211–2221.
[21] M. Fernández-Torrijos, C. Marugán-Cruz, C. Sobrino, D. Santana, C. Richter, Experimental test of tubular external molten salt receivers under non-steady state conditions, AIP Conf. Proc. 2126 (2019).

[22] M. Fernández-Torrijos, C. Sobrino, J.A. Almendros-Ibáñez, C. Marugán-Cruz, D. Santana, Inverse heat problem of determining unknown surface heat flux in a molten salt loop, Int. J. Mass Transf. 139 (2019) 503–516.
[23] M. Fernández-Torrijos, C. Sobrino, C. Marugán-Cruz, D. Santana, Experimental and numerical study of the heat transfer process during the startup of molten salt tower receivers, Appl. Therm. Eng. 178 (2020), 115528.
[24] M.R. Rodríguez-Sánchez, A. Pueyo-Balsells, A. Montoya, J.A. Artero-Guerrero, Solar simulator based on induction heating to characterize experimentally tubular solar central receivers, Appl. Therm. Eng. 220 (2023), 119781.
[25] H. Zhou, Y. Zuo, Y. Li, M. Zhou, Analysis of thermal performance and thermal stress using two-dimensional thermoelastic model for a 50MWe external cylindrical solar receiver, J. Mech. Sci. Technol. (2021).
[26] E.N. Sieder, G.E. Tate, Heat transfer and pressure drop of liquids in tubes, Ind. Eng. Chem. 28 (1936) 1429–1435.
[27] W.R. Logie, J.D. Pye, J. Coventry, Thermoelastic stress in concentrating solar receiver tubes: a retrospect on stress analysis methodology, and comparison of salt and sodium, Sol. Energy 160 (2018) 368–379.